

# Scanning Probe Techniques to Study Interfacial Phenomena at the Nanoscale Level

Lead Guest Editor: Zhichao Lou

Guest Editors: Kun Wang, Quanzhen Zhang, and Yangang Pan





---

**Scanning Probe Techniques to Study  
Interfacial Phenomena at the Nanoscale Level**

Scanning

---

**Scanning Probe Techniques to Study  
Interfacial Phenomena at the Nanoscale  
Level**

Lead Guest Editor: Zhichao Lou

Guest Editors: Kun Wang, Quanzhen Zhang, and  
Yangang Pan



---


Copyright © 2023 Hindawi Limited. All rights reserved.


This is a special issue published in "Scanning." All articles are open access articles distributed under the Creative Commons Attribution License, which permits unrestricted use, distribution, and reproduction in any medium, provided the original work is properly cited.

# Chief Editor

Guosong Wu, China

## Associate Editors


Richard Arinero , France

Daniele Passeri , Italy

Andrea Picone , Italy


## Academic Editors

David Alsteens, Belgium


Igor Altfeder , USA

Jose Alvarez , France

Lavinia C. Ardelean , Romania

Renato Buzio , Italy

J. Chen, Canada

Ovidiu Cretu , Japan

Nicolas Delorme , France


Hendrix Demers , Canada

Jonathan R. Felts, USA


Marina I. Giannotti, Spain

Federico Grillo , United Kingdom


Anton V. Ievlev , USA

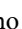
Heng Bo Jiang , China

Berndt Koslowski , Germany

Jessem Landoulsi , France


Jason L. Pitters , Canada

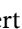
Michela Relucenti , Italy

Francesco Ruffino , Italy

Senthil Kumaran Selvaraj , India

Stefan G. Stanciu, Romania

Andreas Stylianou , Cyprus

Christian Teichert , Austria


Marilena Vivona , United Kingdom

Shuilin Wu, China

## Contents

---

**Microstructure and Mechanical Properties of Gradient Nanostructured Q345 Steel Prepared by Ultrasonic Severe Surface Rolling**

Chao Ge, Weilong Meng, Handui Feng, Muchun Cui, Lei Dong, Tianfeng Miao, Yantong Huo, Jiemin Wu, and Jing Han 




Research Article (7 pages), Article ID 7705844, Volume 2023 (2023)

**Developments of Interfacial Measurement Using Cavity Scanning Microwave Microscopy**

Zhenrong Zhang , Huanfei Wen , Liangjie Li , Tao Pei , Hao Guo , Zhonghao Li , Jun Tang , and Jun Liu 

Review Article (15 pages), Article ID 1306000, Volume 2022 (2022)

**Raman Spectroscopy-Assisted Characterization of Nanoform MoS<sub>2</sub> Thin Film Transistor**

Rajasekaran Saminathan , Haitham Hadidi, Mohammed Tharwan , Ali Alnujaie, Jabril A. Khamaj, and Gunasekaran Venugopal 

Research Article (6 pages), Article ID 3255615, Volume 2022 (2022)

## Research Article

# Microstructure and Mechanical Properties of Gradient Nanostructured Q345 Steel Prepared by Ultrasonic Severe Surface Rolling

Chao Ge,<sup>1</sup> Weilong Meng,<sup>2,3</sup> Handui Feng,<sup>1</sup> Muchun Cui,<sup>1</sup> Lei Dong,<sup>1</sup> Tianfeng Miao,<sup>1</sup> Yantong Huo,<sup>1</sup> Jiemin Wu,<sup>1</sup> and Jing Han<sup>2,3</sup> 

<sup>1</sup>Xuzhou XCMG Mining Machinery Co. LTD, Xuzhou 221000, China

<sup>2</sup>CUMT-XCMG Mining Intelligent Equipment Technology Research Institute, China University of Mining and Technology, Xuzhou 221116, China

<sup>3</sup>School of Mechanical and Electrical Engineering, China University of Mining and Technology, Xuzhou 221116, China

Correspondence should be addressed to Jing Han; hanjing@cumt.edu.cn

Received 19 July 2022; Accepted 10 October 2022; Published 17 April 2023

Academic Editor: Zhichao Lou

Copyright © 2023 Chao Ge et al. This is an open access article distributed under the Creative Commons Attribution License, which permits unrestricted use, distribution, and reproduction in any medium, provided the original work is properly cited.

In this work, ultrasonic severe surface rolling (USSR), a new surface nanocrystallization technique, is used to prepare gradient nanostructure (GNS) on the commercial Q345 structural steel. The microstructure of the GNS surface layer is characterized by employing EBSD and TEM, and the result indicates that a nanoscale substructure is formed at the topmost surface layer. The substructures are composed of subgrains and dislocation cells and have an average size of 309.4 nm. The GNS surface layer after USSR processing for one pass has a thickness of approximately 300  $\mu\text{m}$ . The uniaxial tensile measurement indicates that the yield strength of the USSR sample improves by 25.1% compared to the as-received sample with slightly decreased ductility. The nanoscale substructure, refined grains, high density of dislocations, and hetero-deformation-induced strengthening are identified as responsible for the enhanced strength. This study provides a feasible approach to improving the mechanical properties of structural steel for wide applications.

## 1. Introduction

As common low-alloy steel, Chinese standard Q345 steel exhibits medium strength, good plasticity, and good weldability and is thus widely used in engineering machinery, ships, bridges, steel buildings, pressure vessels, offshore platforms, and other applications. Q345 steel is similar to ASTM A572 grade 50 steel in the U.S. and European standard S355 steel in Europe in terms of its mechanical properties. However, improved strength without visibly sacrificed plasticity is needed for Q345 steel to meet the high-strength requirement of key components or local regions of key components.

Constructing gradient nanostructures (GNSs) have been proven to be a good strategy for enhancing the mechanical properties of metals and alloys inspired by nature [1, 2]. Over the past two decades, this strategy has been successfully applied in almost all types of structural metallic materials

[3–7], such as Cu and Cu alloys [8, 9], Mg alloys [10, 11], and Ti alloys [12, 13]. Several methods have been developed to prepare the gradient nanostructure, such as surface mechanical grinding treatment (SMGT) [3], surface mechanical attrition treatment (SMAT) [14], surface mechanical rolling treatment (SMRT) [15], laser shock peening (LSP) [16], ultrasonic surface rolling (USR), or ultrasonic nanocrystalline surface modification (UNSM) [17–20]. Among these, USR is an effective and easy-to-operate method that has been applied in several steels. Ye et al. [21] applied USR on a 40 Cr (a medium carbon alloy steel) and generated a GNS with a grain size of 3–7 nm in the topmost surface layer, leading to a 52.6% improvement in surface microhardness. However, the strength and plasticity of the GNS 40 Cr were not involved. Liu et al. [22] found that UNSM induced a GNS in AISI 304 stainless steel as well as gradient martensite content, and the average grain size in

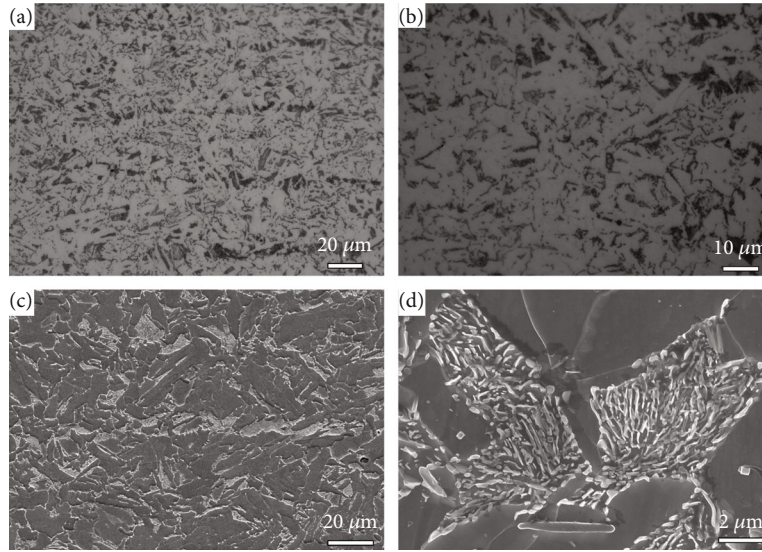


FIGURE 1: The OM (a, b) and SEM (c, d) images of the as-received sample.

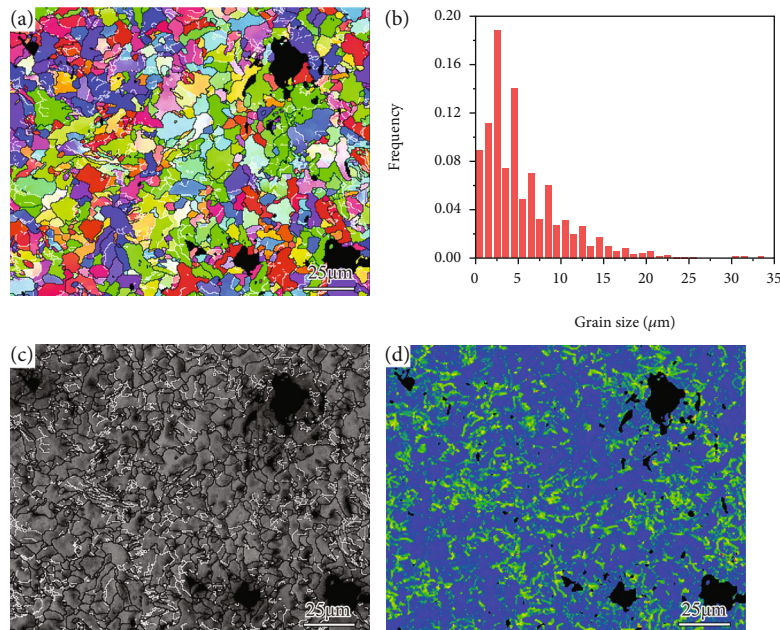


FIGURE 2: The EBSD result of the as-received sample: (a) IPF map, (b) grain size statistics, (c) BC map, and (d) KAM map. The black and white lines in (a, c) profile the HAGBs and LAGBs, respectively.

the topmost surface layer was 4.1 nm. After UNSM, the strength of AISI 304 stainless steel improved from 340 MPa to 630 MPa while still preserving high ductility. Recently, a modified USSR method, called ultrasonic severe surface rolling (USSR), was proposed by Han et al. to obtain a superior gradient surface layer [10]. USSR produces a high strain rate of approximately  $10^5/s$ , which is much higher than many other techniques of preparing GNSs, such as SMAT ( $10^2\sim 10^3/s$ ), SMGT ( $10^3\sim 10^4/s$ ), and SMRT ( $10^3\sim 10^4/s$ ) [2, 10]. USSR applies a large static force on the treated surface for forming a large gradient plastic strain. The large strain and high strain rate enable a thick gradient nanostructure and superior mechanical properties for vari-

ous metals and alloys. Also, USSR synchronously prepares a high-quality surface with low roughness and few processing defects. Our previous work found that USSR forms a gradient structured surface layer with a thickness of  $\sim 1$  mm in the selective laser melted (SLM) 316L stainless steel, endowing the steel with improved strength without a significant loss in ductility as well as enhanced corrosion resistance in NaCl solution [22, 23].

In the present study, USSR is applied to commercial Q345 structural steel to improve its mechanical properties by forming a GNS. The detailed microstructure of the USSR sample was characterized by electron backscatter diffraction (EBSD) and transmission electron microscopy (TEM), and



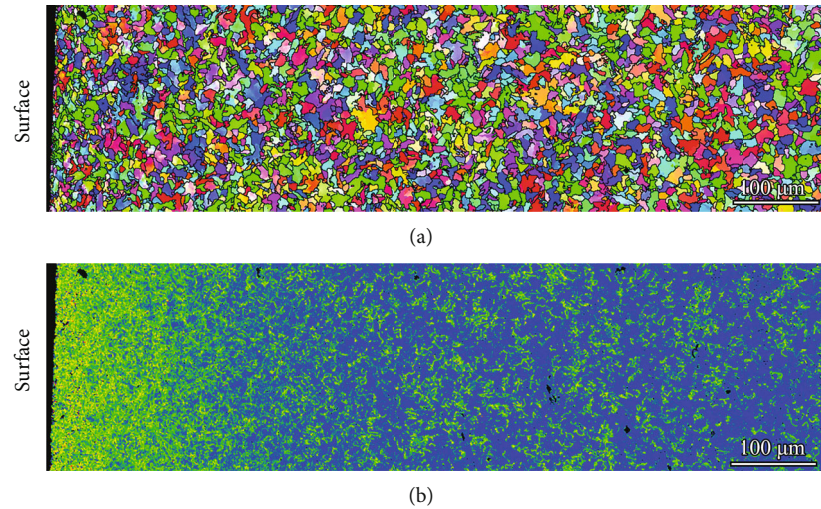


FIGURE 3: Cross-sectional EBSD result of the USSR sample: (a) IPF map and (b) KAM map. The black lines in (a) profile the HAGBs.

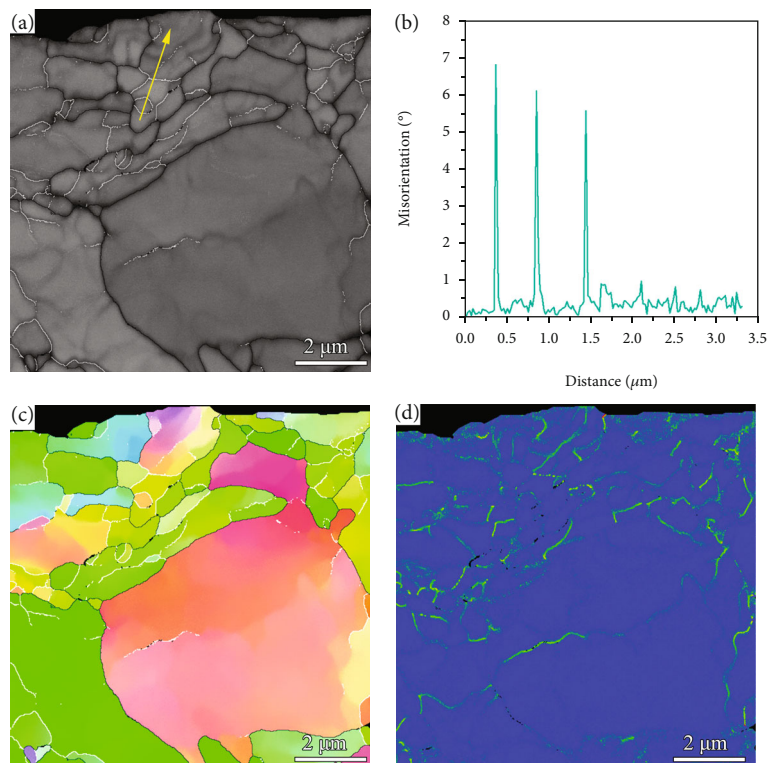


FIGURE 4: High-magnification EBSD result of the USSR sample in the topmost surface: (a) BC image, (b) misorientation change along the arrow in (a), (c) IPF map, and (d) KAM map. Black and white lines in (a, c) profile the HAGBs and LAGBs, respectively.

an attempt was made to link the microstructure to the improved mechanical properties.

## 2. Methods

A commercial hot-rolled Q345 steel plate was used as the initial material. The as-received plate was machined into sheets  $50 \text{ mm} \times 25 \text{ mm} \times 4 \text{ mm}$  in size and then processed by one pass of USSR on two parallel surfaces at room temperature. The process parameters can be found in our previous work [22], but a relatively small static force of 600 N was

applied in this study. During USSR processing, the cutting fluid was used to cool and reduce friction.

The microstructure of the as-received sample was characterized by an optical microscope (OM), scanning electron microscopy (SEM, Hitachi Regulus8100), and EBSD (Oxford Instrument C-Nano). The depth-dependent microstructure of the USSR sample was observed by cross-section EBSD observation. The microstructure of the topmost surface layer was further characterized by TEM (FEI Talos F200X).

The microhardness profile along the depth of the as-received and USSR samples was measured by a Vickers

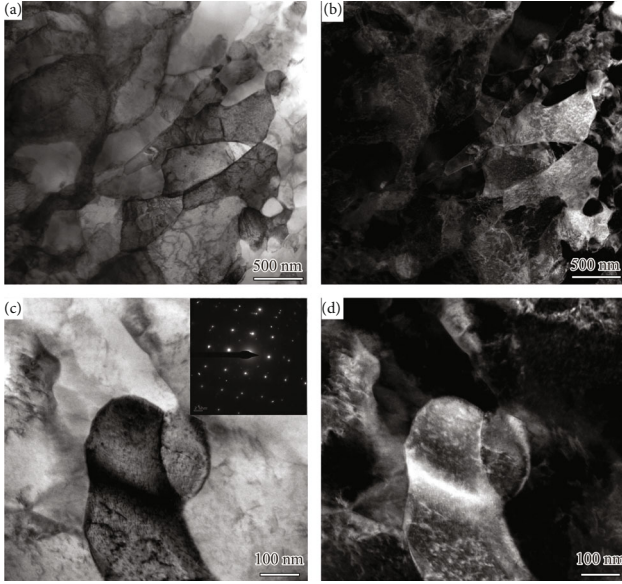


FIGURE 5: TEM images of the USSR sample in the topmost surface layer: (a, b) high-magnification images and (c, d) low-magnification images under (a, c) bright-field and (b, d) dark-field models.

hardness tester. The applied load and duration time were 0.49 N and 10 s, respectively. The mechanical properties were examined through the uniaxial tensile test at room temperature at a speed of 0.5 mm/min. The tensile specimens had a gauge length of 7.5 mm and original width of 2 mm.

### 3. Results

The OM and SEM images indicate that the as-received sample is composed of ferrite and a small amount of pearlite, as indicated in Figure 1. The EBSD inverse pole figure (IPF) and bond contrast (BC) maps show that the ferrite has an average grain size of  $5.6 \mu\text{m}$  and contains a few low angle grain boundaries (LAGBs), as shown in Figure 2. The high kernel average misorientation (KAM) values in some grains imply that the as-received sample involves some lattice defects (Figure 2(d)), most of which are dislocations in this material.

Figure 3 presents the cross-sectional EBSD result of the USSR sample and shows a gradient structure. The grains in the surface layer are refined. The KAM values in the surface layer are significantly higher than those in the matrix and gradually decrease with increasing depth, manifesting decreased defect density, as shown in Figure 3(b). According to the KAM map, the gradient layer has a depth of approximately  $300 \mu\text{m}$ . To further characterize the microstructure of the USSR sample, high-magnification EBSD observation is conducted on the  $10 \mu\text{m}$  thick surface layer, as shown in Figure 4. The BC and IPF maps demonstrate that the ferrite grains separated by high angle grain boundaries (HAGBs) are refined to approximately  $1.5 \mu\text{m}$  and contain many nanoscale substructures. Most substructure boundaries exhibit a misorientation range of  $2\text{--}15^\circ$ , indicating that they are LAGBs, as shown in Figures 4(b) and 4(c), while the misorientations of some substructure boundaries are less than

$2^\circ$ , indicating that these boundaries belong to dense dislocation walls (DDWs). Therefore, the observed nanoscale substructures are composed of subgrains and dislocation cells.

TEM observation was further performed to reveal the detailed microstructure of the topmost surface layer, as depicted in Figure 5. The TEM images and the selected area electron diffraction (SAED) pattern confirm that the large ferrite grains are separated by many substructures composed of subgrains and a small number of dislocation cells. Many dislocations are still visible within these substructures. A small number of nanograins are visible. The average size of the substructures is  $309.4 \text{ nm}$ . Based on the EBSD and TEM observation, a GNS surface layer is formed in the USSR sample.

Figure 6 presents the variation of microhardness along an increasing depth of the investigated samples. The as-received sample has an almost invariable hardness along its depth. A gradually decreased microhardness is observed from the one USSR-treated surface to the matrix in the USSR sample, which results in a U-shaped hardness profile. The gradient hardness profile must be, in our view, a result of the gradient nanostructure. The thickness of the gradient layer is estimated to be  $300 \mu\text{m}$  from the hardness profile, which is consistent with EBSD observations.

Figure 7 presents the typical engineering stress-strain curves of the as-received and USSR samples. The as-received sample has a yield strength of  $379.7 \pm 15.0 \text{ MPa}$ , an ultimate tensile strength of  $527.3 \pm 14.7 \text{ MPa}$ , and an elongation of  $0.36 \pm 0.02$ . The USSR sample exhibits a yield strength of  $474.9 \pm 7.1 \text{ MPa}$ , an ultimate tensile strength of  $551.4 \pm 10.1 \text{ MPa}$ , and an elongation of  $0.32 \pm 0.001$ . This means that the yield strength of the USSR sample improves by 25.1% and is accompanied by a slightly reduced ductility.

### 4. Discussions

*4.1. Strengthening Mechanism.* Through our microstructure characterization, substructure boundary strengthening, grain boundary strengthening, dislocation strengthening, and hetero-deformation-induced (HDI) strengthening are identified as responsible for the high strength of the GNS surface layer. The GNS surface layer is mainly composed of the nanoscale substructures, which are very different from the nanograin structure in previous GNS which involves a large fraction of HAGBs [24–26]. The substructures are mainly separated by LAGBs and DDWs. These substructure boundaries can hinder dislocation motion like HAGBs, while their barrier effect is weaker than the latter due to their small misorientation ( $<2^\circ$ ). Therefore, the substructure boundaries have a relatively weaker strengthening effect, but less sacrificed ductility, which explains the origin of the high strength and good ductility of the USSR sample to a certain extent. The strengthening contribution of LAGBs  $\sigma_{\text{LAGB}}$  can be estimated using Taylor strengthening effect related to the average misorientation [27, 28]:

$$\sigma_{\text{LAGB}} = M\alpha Gb \sqrt{\rho_0 + \frac{3f\bar{\theta}_{\text{LAGB}}}{bd}}, \quad (1)$$

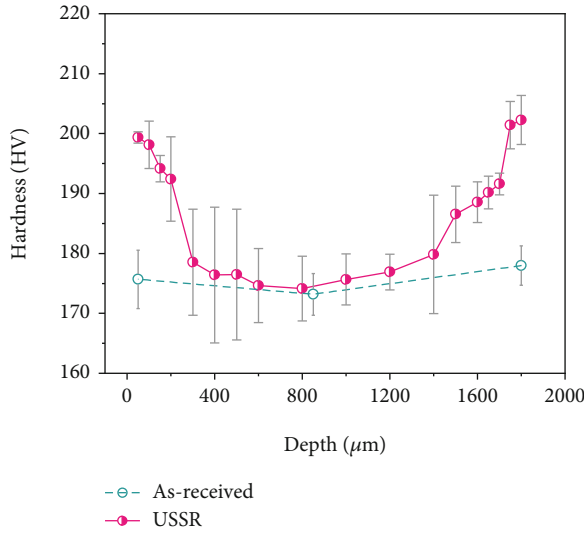


FIGURE 6: Variation of microhardness along the increasing depth of the as-received and USSR samples.

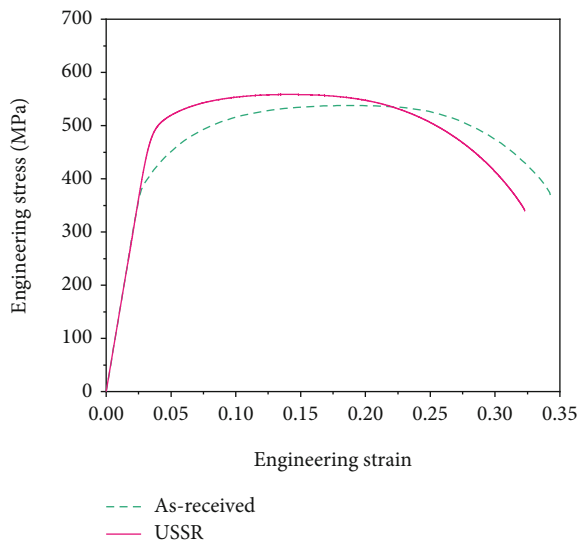


FIGURE 7: Engineering stress-strain curves of as-received and USSR samples.

where  $M$  is the Taylor factor (3.06) and  $\alpha$  is a constant (0.25).  $G$  represents the shear modulus and 80 GPa for steel [29], and  $b$  is the modulus of the Burgers vector of the gliding dislocation (0.25 nm for steel [29]).  $\rho_0$  is the dislocation density between the boundaries and less than  $10^{12}$  [28].  $\bar{\theta}_{LAGB}$ ,  $f$ , and  $d$  present the average misorientation, fraction, and boundary space of LAGBs, respectively, which can be extracted from the EBSD data. Based on our EBSD result of the 10  $\mu\text{m}$  thick surface layer (Figure 4),  $\sigma_{LAGB}$  is as high as 490.58 MPa in this topmost surface layer. The grains separated by HAGBs in the GNS surface layer are slightly refined, thus contributing to enhanced strength through the grain boundary strengthening effect. However, this contributor is relatively small because the grain refinement is not obvious. The GNS surface layer also involves a high den-

sity of dislocations (Figures 3–5), which also contributes to strength improvement by obstructing dislocation motion. As a type of heterostructured material [30, 31], GNSs can induce an HDI-strengthening effect through mechanical incompatibility. The GNS also provides extra work hardening capacity, i.e., HDI hardening, which is regarded as the primary source origin of high ductility [32].

**4.2. Formation of the GNS Surface Layer.** Our microstructure characterization shows that the microstructure of the GNS layer is featured by refined grains, subgrains, dislocation cells, and dense dislocations, and no deformation twins are observed. Hence, the plastic deformation of the Q345 steel is mediated by dislocation activation. Based on previous literature [33, 34], it is suggested that the microstructure refinement of the Q345 steel induced by the USSR is operated through dislocation subdivision, which facilitates the formation of the GNS surface layer. During USSR processing, massive dislocations are activated to accommodate plastic strain and gradually develop DDWs. Prevailing DDWs subdivide the original ferrite grains into individual dislocation cells. Increasing plastic strain, DDWs gradually evolve into LAGBs through dislocation annihilation and rearrangement, leading to the formation of subgrains. Further increasing plastic strain, LAGBs transform into HAGBs, giving rise to grain refinement. This grain refinement process is similar to pure Fe and ferrite in other steels [33, 34]. Here, one pass of the USSR is performed with a relatively small static force, leading to small plastic deformation. Therefore, the substructures but not nanograins are prevailing in the GNS surface layer. More systematic experiments are needed to reveal the relationship between the process parameters of the USSR and the microstructure.

## 5. Conclusions

In the present work, a GNS surface layer is prepared on a commercial Q345 structural steel through one pass of the USSR. Nanoscale substructures composed of subgrains and dislocation cells are formed at the topmost surface layer. The GNS surface layer has a thickness of approximately 300  $\mu\text{m}$ . The uniaxial tensile measurement indicates that the yield strength of the USSR sample improves by 25.1% compared to the as-received sample, with a slightly decreased ductility. The nanoscale substructure, refined grains, high density of dislocations, and HDI strengthening are identified to be responsible for the enhanced strength of the USSR sample.

## Data Availability

Data is available on request.

## Conflicts of Interest

The authors declare that they have no known competing financial interests or personal relationships that could have appeared to influence the work reported in this paper.

## Acknowledgments

This work was financially supported by the CUMT-XCMG Mining Intelligent Equipment Technology Research Project (H7E210025).









## References

- [1] Z. Lou, X. Han, J. Liu et al., "Nano-Fe<sub>3</sub>O<sub>4</sub>/bamboo bundles/phenolic resin oriented recombination ternary composite with enhanced multiple functions," *Composites Part B: Engineering*, vol. 226, article 109335, 2021.
- [2] X. Li, L. Lu, J. Li, X. Zhang, and H. Gao, "Mechanical properties and deformation mechanisms of gradient nanostructured metals and alloys," *Nature Reviews Materials*, vol. 5, no. 9, pp. 706–723, 2020.
- [3] H. W. Huang, Z. B. Wang, J. Lu, and K. Lu, "Fatigue behaviors of AISI 316L stainless steel with a gradient nanostructured surface layer," *Acta Materialia*, vol. 87, pp. 150–160, 2015.
- [4] Y. T. Sun, X. Kong, and Z. B. Wang, "Superior mechanical properties and deformation mechanisms of a 304 stainless steel plate with gradient nanostructure," *International Journal of Plasticity*, vol. 155, article 103336, 2022.
- [5] K. Li, X. Wu, L. Chen et al., "Residual stress and microstructure characterization of 34CrMo<sub>4</sub> steel modified by shot peening," *Scanning*, vol. 2020, Article ID 5367345, 8 pages, 2020.
- [6] K. Li, Q. Zheng, C. Li et al., "Characterization of surface modification of 347 stainless steel upon shot peening," *Scanning*, vol. 2017, Article ID 2189614, 4 pages, 2017.
- [7] Q. Zheng, K. Li, X. Yin et al., "Corrosion properties of 34CrMo<sub>4</sub> steel modified by shot peening," *Scanning*, vol. 2017, Article ID 1928198, 8 pages, 2017.
- [8] Y. F. Wang, C. X. Huang, M. S. Wang, Y. S. Li, and Y. T. Zhu, "Quantifying the synergetic strengthening in gradient material," *Scripta Materialia*, vol. 150, pp. 22–25, 2018.
- [9] T. H. Fang, W. L. Li, N. R. Tao, and K. Lu, "Revealing extraordinary intrinsic tensile plasticity in gradient nano-grained copper," *Science*, vol. 331, no. 6024, pp. 1587–1590, 2011.
- [10] J. Han, J. Sun, Y. Song et al., "Achieving gradient heterogeneous structure in Mg alloy for excellent strength-ductility synergy," *Journal of Magnesium and Alloys*, 2021.
- [11] J. Han, C. Wang, Y. Song, Z. Liu, J. Sun, and J. Zhao, "Simultaneously improving mechanical properties and corrosion resistance of as-cast AZ91 Mg alloy by ultrasonic surface rolling," *International Journal of Minerals, Metallurgy, and Materials*, vol. 29, no. 8, pp. 1551–1558, 2022.
- [12] X. Li, B. Sun, B. Guan et al., "Elucidating the effect of gradient structure on strengthening mechanisms and fatigue behavior of pure titanium," *International Journal of Fatigue*, vol. 146, article 106142, 2021.
- [13] C. Liu, D. Liu, X. Zhang et al., "Improving fatigue performance of Ti-6Al-4V alloy via ultrasonic surface rolling process," *Journal of Materials Science and Technology*, vol. 35, no. 8, pp. 1555–1562, 2019.
- [14] X. H. Chen, J. Lu, L. Lu, and K. Lu, "Tensile properties of a nanocrystalline 316L austenitic stainless steel," *Scripta Materialia*, vol. 52, no. 10, pp. 1039–1044, 2005.
- [15] W. Xu, X. C. Liu, and K. Lu, "Strain-induced microstructure refinement in pure Al below 100 nm in size," *Acta Materialia*, vol. 152, pp. 138–147, 2018.
- [16] J. Z. Lu, K. Y. Luo, Y. K. Zhang et al., "Grain refinement mechanism of multiple laser shock processing impacts on ANSI 304 stainless steel," *Acta Materialia*, vol. 58, no. 16, pp. 5354–5362, 2010.
- [17] X. Teng, Y. Jia, C. Gong, C. Zhang, X. Zhang, and S. Tu, "Effect of ultrasonic surface deep rolling combined with oxygen boost diffusion treatment on fatigue properties of pure titanium," *Scientific Reports*, vol. 11, no. 1, 2021.
- [18] O. Unal, E. Maleki, I. Karademir, F. Husem, Y. Efe, and T. Das, "The formation of gradient nanostructured medium carbon steel via mild, moderate, and severe ultrasonic nanocrystal surface modification options: Assessment on wear and friction performance," *Materials Science and Engineering B-Advanced Functional Solid-state Materials*, vol. 285, article 115970, 2022.
- [19] H. H. Lee, H. K. Park, J. Jung, A. Amanov, and H. S. Kim, "Multi-layered gradient structure manufactured by single-roll angular-rolling and ultrasonic nanocrystalline surface modification," *Scripta Materialia*, vol. 186, pp. 52–56, 2020.
- [20] W. Ting, W. Dongpo, L. Gang, G. Baoming, and S. Ningxia, "Investigations on the nanocrystallization of 40Cr using ultrasonic surface rolling processing," *Applied Surface Science*, vol. 255, no. 5, pp. 1824–1829, 2008.
- [21] C. Ye, A. Telang, A. S. Gill et al., "Gradient nanostructure and residual stresses induced by ultrasonic nano-crystal surface modification in 304 austenitic stainless steel for high strength and high ductility," *Materials Science and Engineering: A*, vol. 613, pp. 274–288, 2014.
- [22] Y. Liu, J. Sun, Y. Fu et al., "Tuning strength-ductility combination on selective laser melted 316L stainless steel through gradient heterogeneous structure," *Additive Manufacturing*, vol. 48, article 102373, 2021.
- [23] J. Sun, Q. Sun, Y. Liu et al., "Improving corrosion resistance of selective laser melted 316L stainless steel through ultrasonic severe surface rolling," *Journal of Materials Research and Technology*, vol. 20, pp. 4378–4391, 2022.
- [24] X. Wang, Y. S. Li, Q. Zhang, Y. H. Zhao, and Y. T. Zhu, "Gradient structured copper by rotationally accelerated shot peening," *Journal of Materials Science and Technology*, vol. 33, no. 7, pp. 758–761, 2017.
- [25] Z. Zhou, S. Wang, J. Li, Y. Li, X. Wu, and Y. Zhu, "Hardening after annealing in nanostructured 316L stainless steel," *Nano Materials Science*, vol. 2, no. 1, pp. 80–82, 2020.
- [26] C. Wang, K. Luo, J. Wang, and J. Lu, "Carbide-facilitated nanocrystallization of martensitic laths and carbide deformation in AISI 420 stainless steel during laser shock peening," *International Journal of Plasticity*, vol. 150, article 103191, 2022.
- [27] J. Sun, B. Li, J. Yuan et al., "Developing a high-performance Mg-5.7Gd-1.9Ag wrought alloy via hot rolling and aging," *Materials Science and Engineering: A*, vol. 803, article 140707, 2020.
- [28] P. Luo, D. T. McDonald, W. Xu, S. Palanisamy, M. S. Dargusch, and K. Xia, "A modified Hall-Petch relationship in ultrafine-grained titanium recycled from chips by equal channel angular pressing," *Scripta Materialia*, vol. 66, no. 10, pp. 785–788, 2012.
- [29] M. Huang, P. E. J. Rivera-Díaz-Del-Castillo, O. Bouaziz, and S. van der Zwaag, "Modelling strength and ductility of ultrafine grained BCC and FCC alloys using irreversible thermodynamics," *Materials Science and Technology*, vol. 25, no. 7, pp. 833–839, 2009.

- [30] Y. Zhu, K. Ameyama, P. M. Anderson et al., "Heterostructured materials: superior properties from hetero-zone interaction," *Materials Research Letters*, vol. 9, no. 1, pp. 1–31, 2021.
- [31] B. Xu, J. Sun, Z. Yang et al., "Wear behavior of the multiheterostructured AZ91 mg alloy prepared by ECAP and aging," *Scanning*, vol. 2020, Article ID 4873286, 10 pages, 2020.
- [32] Y. Hu and X. Wu, "Perspective on hetero-deformation induced (HDI) hardening and back stress," *Materials Research Letters*, vol. 10, pp. 393–398, 2019.
- [33] N. R. Tao, Z. B. Wang, W. P. Tong, M. L. Sui, J. Lu, and K. Lu, "An investigation of surface nanocrystallization mechanism in Fe induced by surface mechanical attrition treatment," *Acta Materialia*, vol. 50, no. 18, pp. 4603–4616, 2002.
- [34] L. Zhou, G. Liu, X. L. Ma, and K. Lu, "Strain-induced refinement in a steel with spheroidal cementite subjected to surface mechanical attrition treatment," *Acta Materialia*, vol. 56, no. 1, pp. 78–87, 2008.

## Review Article

# Developments of Interfacial Measurement Using Cavity Scanning Microwave Microscopy

Zhenrong Zhang <sup>1,2,3</sup> Huanfei Wen <sup>1,2,3</sup> Liangjie Li <sup>1,2,3</sup> Tao Pei <sup>1,2,3</sup> Hao Guo <sup>1,2,3</sup>  
Zhonghao Li <sup>1,2,3</sup> Jun Tang <sup>1,2,3</sup> and Jun Liu <sup>1,2,3</sup>

<sup>1</sup>Key Laboratory of Instrument Science and Dynamic Testing Ministry of Education, North University of China, Taiyuan 030051, China

<sup>2</sup>Key Lab of Quantum Sensing and Precision Measurement, Shanxi Province, Taiyuan 030051, China

<sup>3</sup>Institute of Instrument and Electronics, North University of China, Taiyuan 030051, China

Correspondence should be addressed to Jun Tang; tangjun@nuc.edu.cn and Jun Liu; liuj@nuc.edu.cn

Received 18 April 2022; Revised 21 June 2022; Accepted 15 July 2022; Published 12 August 2022

Academic Editor: Zhichao Lou

Copyright © 2022 Zhenrong Zhang et al. This is an open access article distributed under the Creative Commons Attribution License, which permits unrestricted use, distribution, and reproduction in any medium, provided the original work is properly cited.

In the field of materials research, scanning microwave microscopy imaging has already become a vital research tool due to its high sensitivity and nondestructive testing of samples. In this article, we review the main theoretical and fundamental components of microwave imaging, in addition to the wide range of applications of microwave imaging. Rather than the indirect determination of material properties by measuring dielectric constants and conductivity, microwave microscopy now permits the direct investigation of semiconductor devices, electromagnetic fields, and ferroelectric domains. This paper reviews recent advances in scanning microwave microscopy in the areas of resolution and operating frequency and presents a discussion of possible future industrial and academic applications.

## 1. Introduction

Over the past decade, one of the most significant advances in the field of microwave testing has been the emergence of scanning microwave microscopy [1–9]. There are two main types of scanning microwave microscope, categorized according to the source of the microwave signals at the scanning tip, with one type using a microwave resonator coupled to the tip of the probe using a small aperture and the other using a coaxial transmission line directly attached the tip of the atomic force microscopy (AFM) cantilever. Regardless of whether the small aperture of the probe is contained in a sharp tip or a cavity, the formation of the microwave image is accomplished through the capture of the microwave reflectance either in magnitude or in phase, as well as by the simultaneous probe scanning across the specimen surface [10–13]. In this review, we focus on the resonant cavity-type scanning microwave microscope.

The scanning microwave microscope can be used to study the electromagnetic properties of a sample via an interaction with a nanoscale scanning probe. Scanning microwave microscopy allows quantitative measurements of dielectric constants and losses in materials. The use of this approach enables simultaneous high-speed, noncontact, and nondestructive measurements to be made [14–16]. In some cases, the microwaves can penetrate into the sample, providing opportunities for tomographic analysis [17]. Due to these advantages, scanning microwave microscopy can achieve nanoscale near-field measurements, something of great use in future applications of high-resolution microwave image generation.

In this review, we present recent advances in the research of scanning microwave microscopy. The current progress in applications and development of the technique are reviewed here, including its limitations and advantages, as well as the scope for further developments. The paper begins with a discussion of the basic design and subsequent improvements in

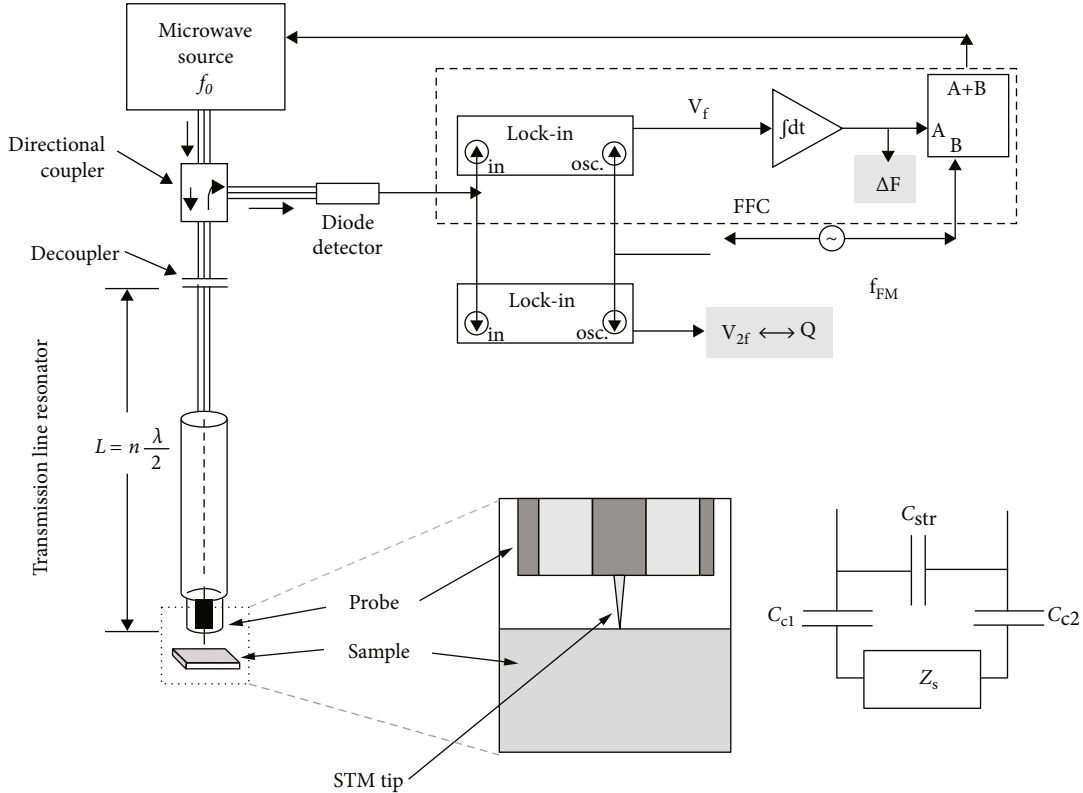


FIGURE 1: Schematic diagram of the key components of a half-wavelength cavity-type near-field scanning microwave microscope.

instrumentation for scanning microwave microscopy. Then current applications of the technique are discussed. Finally, conclusions and a discussion of possible future developments are made.

## 2. Basic Design and Improvements in Instrumentation for Scanning Microwave Microscopy

The use of microwaves permits the generation of decaying or evanescent electromagnetic fields at discontinuities in waveguides and the use of these highly-confined fields for microscopy [18]. This type of microscopy is sometimes referred to as “scanning microwave impedance microscopy” (SMIM), “near-field scanning microwave microscopy” (NSMM), or “near-field microwave microscopy” (NFMM), but here, we will uniformly refer to the technique as “scanning microwave microscopy” (SMM). There are many kinds of signal analysis used to construct the images, such as the change in the Quality ( $Q$ ) factor of the resonant cavity, the change in capacitance between the probe and the sample, the frequency drift, and the  $S_{11}$  and  $S_{21}$  values of the microwave signal. In recent years, most experimental systems have used vector network analyzers to acquire the required signals, although some researchers continue to build their own signal acquisition systems. Materials with different properties cause different obstacles to microwave conduction related to the composition, structure, purity, defect, and impurity content of the samples. This allows microwave microscopy to use changes in the con-

duction of the microwaves in the near-field as a diagnostic test. Using microwaves as a test signal has the advantages that optical and acoustic signals lack, such as strong penetration, no damage to the sample, and short relaxation time.

Current approaches to scanning microwave microscopy follow similar lines. The signal resonates through the resonator, and the field is concentrated by the use of a tip much smaller than the wavelength of the microwaves, resulting in a strong local measurement of the sample [19]. Local storage of part of the signal is noted in the near-zone and evanescent waves. The rest of the signal is partially absorbed by the specimen, partially reflected to the transmission line, and partially dispersed in the form of far-field illumination. The specimen response can be captured by monitoring the height- and position-dependent variations of the reflected or dispersed signals [20]. The reflected microwave signal decays quickly and can be solved analytically using transmission line theory [21–25]. Figure 1 shows the key components of a typical near-field microwave microscope [23].

The microscope consists of a microwave source, a coaxial resonator coupled to the microwave generator (through a decoupling capacitor or inductor), a detector to measure the reflected signal from the resonator, and a frequency-following circuit (FFC) [26]. The instrument shown in Figure 1 uses a half-wavelength resonant cavity, but many scanning microwave microscopes use a four-wavelength resonant cavity, as shown in Figure 2 [20].

This approach uses a significantly faster technology called phase-sensitive detection. By adjusting the phase shifter, the difference in phase between the resonator and a reference

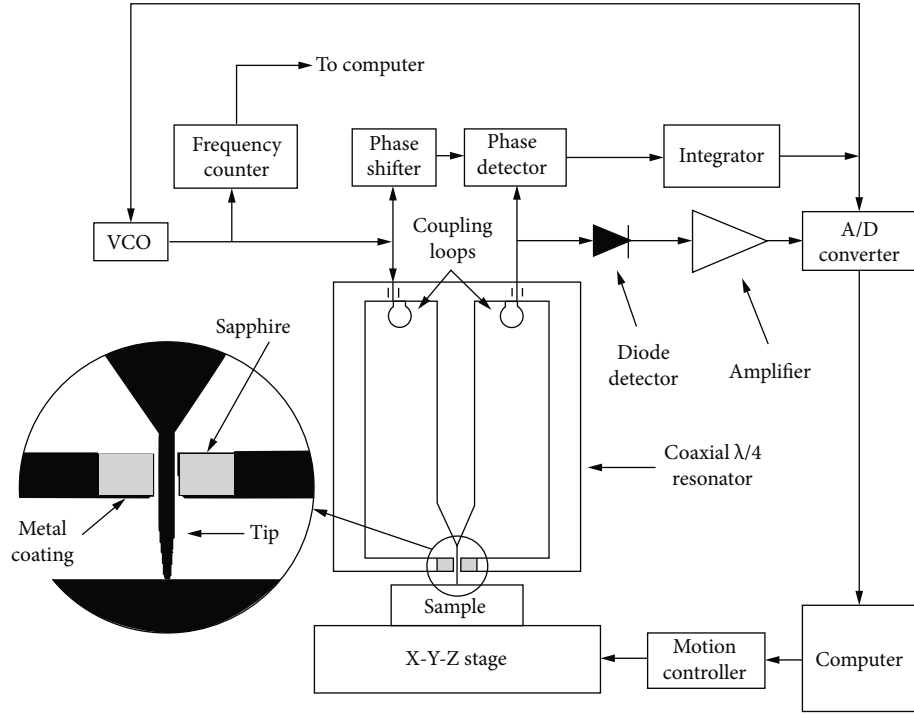


FIGURE 2: Schematic diagram of the key components of a  $\lambda/4$  cavity-type near-field scanning microwave microscope.

signal is made  $90^\circ$  in the absence of the sample under the tip. The amplification, fusion, and subsequent feedback of this signal to the VCO (voltage-controlled oscillator) are made possible by the proportionality of the phase detector output to the magnitude of the phase shift, thereby achieving the oscillator phase locking at  $f_r$ . For quantification of the  $f_r$  shift and  $Q$  under this approach, a diode detector is utilized to separately determine the amplitude of the resonator output signal and the error signal of the phase lock loop. By moving the specimen under the resonator-tip assembly, the acquisition of images is possible while documenting the variations in  $f_r$  and  $Q$ .

A series lumped equivalent resonant circuit in series (Figure 3) can be used to model the SMM system. The angular resonant frequency can be calculated from  $\omega_r = 2\pi f_r = 1/\sqrt{LC}$ , where  $L$  and  $C$  are the effective inductance and capacitance, respectively, and  $f_r$  is the resonant frequency [20, 25]. The impedance of the lumped elements can be used to quantify the sample-tip interaction  $Z_t = R_t + iX_t$ , with  $Z_t$  being a function of the geometry of tip, the distance of the tip from the sample, and the electrodynamic properties of the sample. A detailed theoretical analysis between the tip of the needle and the sample is given in reference [23].

### 3. Early Developments in Scanning Microwave Microscopy

Scanning microwave microscopy is a useful tool for studying the surface and internal structure of materials. It is used to test a variety of physical quantities, including dielectric and ferroelectric dielectrics and the properties of materials such as semiconductors, metals, superconductors, and biological

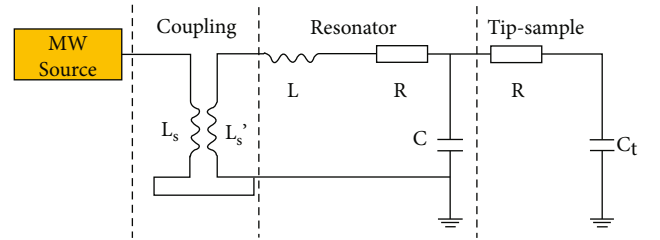


FIGURE 3: Equivalent circuit of a cavity-type near-field scanning microwave microscope.

specimens. However, there are still challenges remaining to its wide-scale adoption, the most significant of which is the existence of a large common-mode signal arising in part from noise. Reducing the noise signal is an area of intense current study to permit the broadening of applications for the technique through higher resolution and clearer images.

Thanawalla et al. [25] proposed a tip-structured probe employing a high-quality resonator and a novel shielding structure to shield the probe tip from far-field components. This permitted the imaging of the dielectric constant and loss tangent of dielectric materials at the spatial resolution of 100 nm and sensitivity of  $\delta\epsilon/\epsilon \approx 1 \times 10^{-5}$ . The quantitative complex electrical impedance microscopy is also possible using model analysis. As microwave wavelengths in metals are four orders of magnitude smaller than those in free space, they did not study metals with their system.

Williams et al. [26] achieved a resolution of 25 nm with their system. They utilized a resonant circuit to provide a method for detecting capacitance changes between the tip and a surface below  $100 \mu\text{m}$  with a sensitivity of  $1 \times 10^{-19}$  F



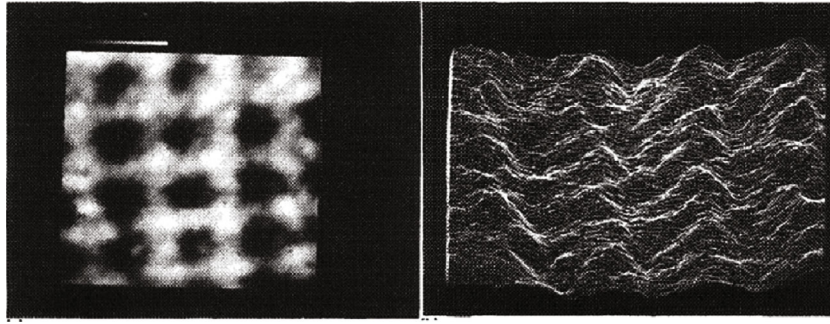


FIGURE 4: Grayscale and line scan capacitance images of an array of 50 nm diameter holes, 50 nm apart. The structure is an 100 nm-thick PMMA film that is overcoated with 20 nm of gold. The field of view of a 370 nm square [26].

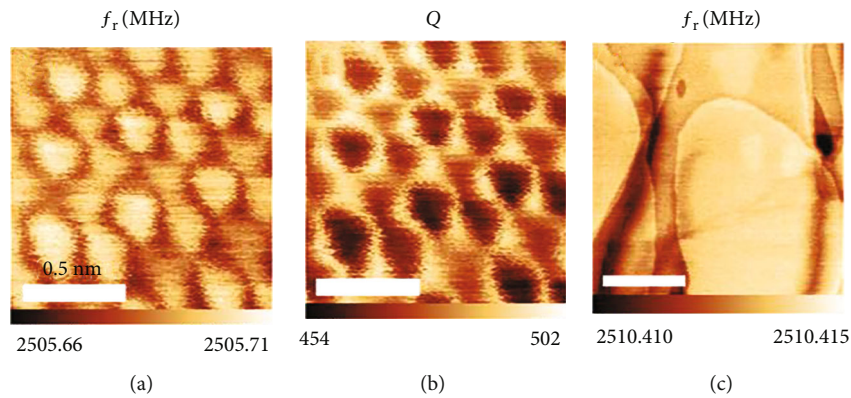


FIGURE 5: A  $300 \times 300 \text{ nm}^2$  area of Au(111), showing the atomic-resolution microwave signal images of  $f_r$  using a hybrid STM/SMM system. The STM bias line and the current preamplifier are disconnected from the setup during SMM imaging [27].

at a bandwidth of 1 kHz. The feedback control circuit was used, and the tip was scanned at a fixed distance from the sample to provide a noncontact method of surface profiling. They presented images of both conducting and nonconducting structures, demonstrating a sensitivity limit for capacitance imaging of below 10 nm, and showing capacitance imaging at the 25 nm scale (Figure 4).

Manassen et al. [27] demonstrated atomic-resolution imaging using a hybrid scanning tunneling/near-field microwave microscope. The microwave channels of the microscope conform to the resonant frequency and quality factor of a coaxial microwave resonator, which is built into the STM scan head and coupled to the probe tip. Figure 5 shows some of the images that they obtained. They found that they could obtain atomic-resolution images by adopting the microwave channel of the  $\mu$ -wave STM provided that the tip sampling distance was within the tunneling state [19]. They conjectured that the atomic contrast in the microwave channels was caused by a GHz frequency current flowing through the tip-sample tunnel junction. They imaged both HOPG and Au(111) surfaces. GHz atomic-resolution images allow material properties such as those arising from elemental selectivity/sensitivity phenomena to be observed, including dielectric relaxation and electron spin resonance [27]. In addition, the MHz bandwidth of the resonators used in this research proved suitable for use in high-speed spectroscopic measurements at the atomic scale.

Biani et al. [28] described the imaging of graphene sheets using a homebuilt double-channel scanning probe microscope that performed both near-field broadband scanning microwave microscopy and STM. They incorporated conversion in the time-domain to generate microwave images of superior quality with nanometric resolution. For the time-domain elucidation of the desired signal, an inverse Fourier transform was implemented. They deposited the graphene specimens on a  $\text{SiO}_2$  substrate and overlaid them with gold. The results appeared to demonstrate a drastic variation in impedance in the vicinity of the flake edges, which probably suggests a build-up of charge.

Jooyoung et al. [29] conceived an SMM system that comprised a coaxial  $\lambda/4$  resonator with a tunable cavity that was coupled to a sharp probe tip. When the operational frequency  $f$  ranged between 1 and 1.5 GHz, they were able to achieve better spatial resolution and sensitivity compared to that of the near-field image ( $4 \mu\text{m}$ ) of a  $\text{YBa}_2\text{Cu}_3\text{O}_y$  film that was deposited on a MgO substrate [29]. By appropriately tuning the length of the resonance cavity, the probe could be made even more sensitive. The spatial resolution and sensitivity variations with the length of the cavity were adjusted using the resonance cavity tuning. This system has the potential to extend the measurement range by extending the frequency range and lowering the operating temperature.

Bertness et al. [30] demonstrated that SMM is suitable for use in determining the photoresponse of photovoltaic materials

whose lateral resolution may be of submicrometer scale. In this approach, an RF-STM (radiofrequency scanning tunneling microscopy) tip is coupled to a microwave cavity, whose resonance frequency is around 4.5 GHz. The load on the cavity is altered by the additional mobile carriers near the tip of the probe. Quantification of these alterations is accomplished by measuring the shifts in the Q factor and resonance frequency. In the case of the GaAs and Cu (In, Ga) Sez solar cell material, the conductivity variation determination under blue light irradiation was easily achievable. As modeling of this behavior improves, this approach should become sensitive enough to quantify the sample conductivity fluctuations on both the absolute and relative scales. The use of SMM for the testing of photovoltaic materials is a very fruitful area of future application, as photovoltaic materials are of increasing importance in the modern world.

Talanov et al. [31] designed a microwave probe for near-field scanning with a sampling diameter of around 10  $\mu\text{m}$ . This is the smallest sample volume yet attained in near-field microwave microscopy and constrains > 99% of the gross sampling reactive energy for the probe so that the response is almost irrelevant to the properties of samples outside this zone. The probe comprises a balanced stripline micrometer-sized resonator (4 GHz) that can carry out noncontact, nondestructive testing. Its applicability to the spatially localized metrology of electrical quantities is especially high.

Tabib-Azar et al. [32] investigated several issues concerning the development of evanescent microwave probes (EMP) and discussed the applicability of such probes in materials research. They determined that these probes were superior in terms of spatial resolution to those with lower dielectric constants and superior in terms of spatial resolution to those with lower permittivity. In the case of magnetic dipole probes, they found that their resolution was not identically reliant on the dielectric constant of the substrate. They attributed this lack of appreciable dependence to the prevailing reliance of the magnetic field curves on the radius of the probe wire loops and the irrelevance of the loop dimension to the permittivity of the substrate. In semiconductors, the use of EMP enabled imaging of the conductivity fluctuation, as well as the recombination lifetime. Their use also allowed the acquisition of the nonuniform behavior of composites, metals, insulators, balsa wood, and a plant leaf. The EMP promises broad applicability in investigating botanical and biological materials, as it achieves the nondestructive and noncontact imaging of these materials via appropriate media like air.

In summary, since the earliest days following its inception, scanning microwave microscopy has found a very wide range of applications in testing material dielectric constants, morphology, optoelectronic materials, biological samples, and so on. Moreover, its increase in resolution, coupled with its nondestructive nature, provided a good research basis for the subsequent development of SMM.

#### 4. Recent Developments in Scanning Microwave Microscopy

In this section, we summarize the recent advances in the use of scanning microwave microscopy to study material prop-

erties, morphology, chip imaging, and biological testing, respectively.

*4.1. Recent Advances in the Use of SMM to Determine Material Properties.* Bakli et al. [11] reported the use of an interferometric procedure in place of classic resonant approaches, which utilized repeated passive devices with superior stability and accuracy. Their fading probe, which has high impedance, is compatible with current metrological measurement systems, and the method has the advantages of being broadband and having high measurement precision and convenience of operation. Using this integration of interferometry and near-field microscopy, they could obtain high measurement sensitivity without using large and expensive resonators. They also developed a new calibration model for relating the near-field reflectance measurement to the local properties of the test sample.

Fecioru-Morariu et al. [33] reported a method for acquiring the distribution diagram of high-frequency conductivity for an oxide-coated ferromagnetic membrane as thin as 200 nm based on the SMM-derived Q. Circuit analog estimation was used to assess the electrical properties for the resonator. The interaction between the sample and tip was modeled using FEA so that the resonant frequency and Q values corresponding to the sample were retrievable [34]. The simulation was verified using a specimen of thin Cu membrane to quantify the simulated Q variation with the conductivity plot. They then explored how the nonmagnetic application of  $\text{Al}_2\text{O}_3$  on AF (antiferromagnetic) IrMn films affected the high-frequency conductivity of the films by calculations that provide high-frequency conductivity values for these thin-film samples.

Imtiaz et al. [35] tested the widely used quasistatic deem bedding procedure for characterizing bulk materials with SMM tips. To properly characterize conducting materials, the extra loss mechanism resulting from the antenna impedance fluctuation into the near-field that was above the plane of the conducting ground must be considered [36–38]. This loss is determined by the material conductivity, and the loss is considerable in the case of materials considerably exceeding  $10^3 \text{ S/m}$  [35]. Quasistatic models were found to be acceptable for fused silica and silicon, as the variation of impedance attributable to the plane boundary proximity with materials was ignorable when the conductivities were below  $10^3 \text{ S/m}$ . They also introduced an SMM-based strategy for material differentiation via complex permittivity magnitude by plotting the variation of the product  $(\Delta f/f_0)(Q/Q_0)$  with the tip height.

*4.2. Testing the Topography of the Material.* Zhang et al. [8] reported a method that could correct the skewing and denoising of SMM images, significantly enhancing the spatial resolution of the images, as can be seen in Figure 6. Through electromagnetic simulation, they obtained the optimal approach to increasing the electric field strength at the tip of the needle. This includes reducing the length of the tip protruding from the coaxial cavity, the distance between the tip and the sample, and the diameter of the tip. They scanned a Cu film grid and compared the half-height widths of the test curves with and without tip optimization to obtain

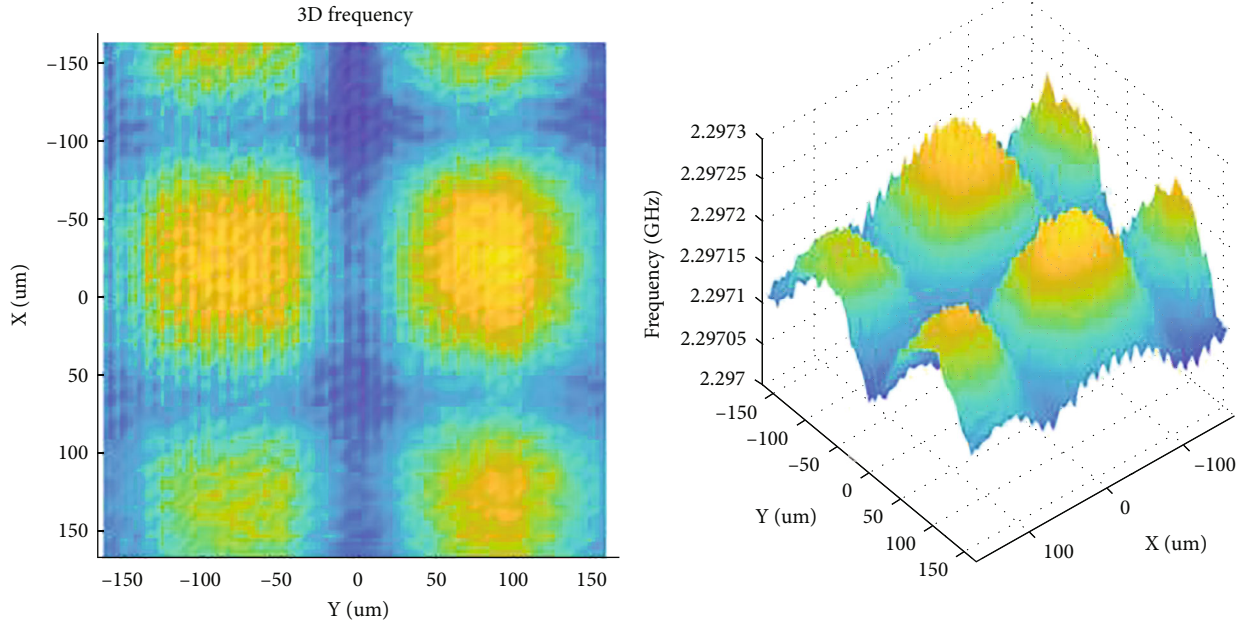


FIGURE 6: An enhanced grid contour image and  $f_r$  parameter image of a copper film after tilt correction [8].

a method for enhancing the sensitivity of the SMM system. The detection sensitivity was greatest when the tip protruded 3 mm from the cavity, the distance between the tip and the sample was  $1.44 \mu\text{m}$ , and the diameter of the tip was  $1.6 \mu\text{m}$ . In addition to the Cu thin-film grid, they also tested  $f_r$ ,  $S_{11}$ , and  $Q$  images of coin textures, lithographic masks, and leaf veins, and the test images became sharper than the originally obtained blurred images using their tilt correction method.

Bagdad et al. [39] designed and fabricated a scanning microwave microscope for characterizing semiconductor structures, as shown in Figure 7. Their SMM system utilizes a homemade coaxial cavity resonator that uses a network analyzer as the signal source. The inner resonator conductor is linked to a sharpened tungsten tip made, which was electrochemically prepared. Semiconductor structural metrics, including the resonance frequency  $f_r$ , the quality factor  $Q$ , the reflection coefficient  $S_{11}$ , and the transmission  $S_{21}$  for the resonant cavity, were scanned with the sharpened tip of the probe while maintaining the tip-sample distance within the near-field zone. Due to the interaction of the probe tip with the test sample, the metric parameters undergo fluctuations, showing correlations with the dielectric properties and topography of the tiny material zone beneath the probe tip. This makes it possible to generate a 2D image of the  $f_r$ ,  $Q$ ,  $S_{11}$ , and  $S_{21}$  parametric progression on the surface of the test sample.

Gao and Xiang [40] used an SMM instrument for measuring the interconnect and interline capacitance in a non-contact mode at the femtofarad level with the aid of a miniature tester device [40]. Their procedure is applicable to the investigation of the variation in electrical parameters in integrated circuit interconnects while generating parameters for subsequent statistical design. They also explored its

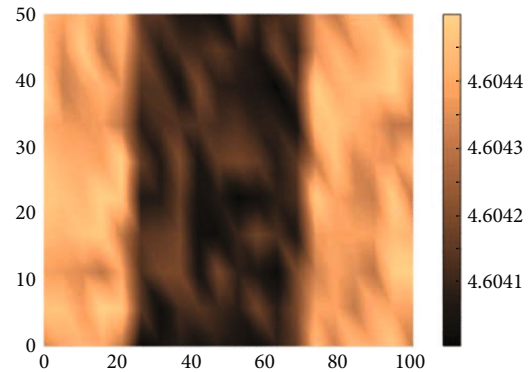


FIGURE 7: The 2D distribution of the resonant frequency (GHz) on a  $50 \mu\text{m}$ -width gold layer deposited on top of a  $\text{SiO}_2/\text{Si}$  substrate [39].



FIGURE 8: Images of the watermark included in a 20 EUR banknote obscured by a metallic mask [42].

applicability to the determination of low-dielectric losses and interconnect line resistance. The geometry of their tester device may be suitable for the microwave elucidation of

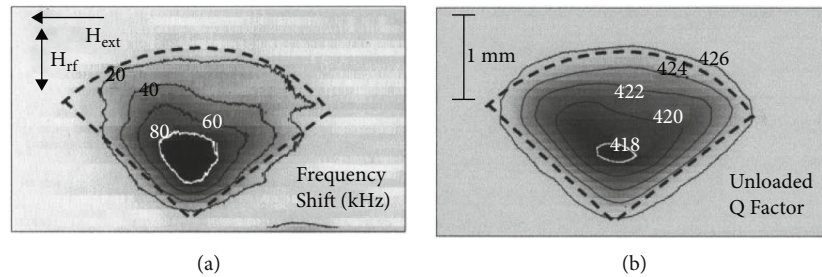


FIGURE 9: Images of an LSMO single-crystal taken at 6.037 GHz at a sample–probe separation of  $10\ \mu\text{m}$ . (a)  $\Delta f$  image of the LSMO sample at an external field  $H_{\text{ext}} = 1317\ \text{Oe}$ , chosen to give a minimum unloaded  $Q$  factor at the center of the sample, and (b) unloaded  $Q$  factor image at an external field  $H_{\text{ext}} = 1411\ \text{Oe}$ , chosen to give a minimum  $\Delta f$  at the center of the sample. A background frequency shift has been subtracted from (a). The dashed line presents the approximate location of the sample [48].

diverse functional nanomaterials, including carbon nanotubes, nanofibers, nanowires, and nanoribbons through the connection of the test object between the 2 interconnect lines.

Gregory et al. [41] utilized a wire probe with a globular tip of a diameter of approximately  $0.1\ \text{mm}$  as a modification of the cavity perturbation type. Given the enrichment of the field at the zone closest to the specimen, the measurement resolution using this probe is on the order of microns, which is considerably less than the diameter of the tip, particularly at a high dielectric constant. They presented both an innovative SMM design and a novel calibration algorithm, as well as a novel calibration reference (polar liquids). They used Laplace “complex frequencies” for the first time in the computational and calibration outcomes, which permitted the accurate measurement of losses in highly lossy materials. In addition, for a microwave microscope having a line probe, a beam deflector was designed.

**4.3. Imaging of the Subsurface of the Sample.** The microwave signal can penetrate certain media to a depth sufficient to obtain subsurface information of the sample. Pearanda-Foix [42] described the use of scanning microwave microscopy techniques to identify security markings on banknotes. Their system included a stand-alone vector network analyzer to allow the reflection response of a near-field coaxial probe to be measured. They combined displacement laser and cavity perturbation techniques to investigate the correlation between the dielectric properties of the sample and the resonant response of the probe. The system was able to measure subsurface subfabricated images, as shown in Figure 8.

**4.4. Imaging of the Local Electric Field Properties of Nanomaterials.** Measurements of the local density of states and local surface resistance can reveal how changes in the local density of states because of impurities, defects, grains, carrier bias, etc., affect local resistance on the nanometer scale [43, 44].

Tadashi et al. [45] measured the local density of states and the local surface resistance in low local surface resistance materials through the local measurements of tunneling spectra and sheet resistance within the boundary region of the gold deposition and nondeposition zones on the HOPG by SMM. Their results showed significant differ-

ences in the local resistance around the boundary as well as differences in the tunneling spectra. They combined their system with STM to measure the local density of states as well as local surface resistance on the nanoscale. Their work demonstrated that this approach is a useful tool to study the effect of local disorder on electrostatics and measure the local properties of nanomaterials.

**4.5. Imaging of the Local Magnetic Properties of Metal Samples.** Magnetic materials are essential materials in modern science and technology [46, 47]. The sensitivity of SMM to magnetic properties makes it suitable for use in testing magnetic materials. Lee et al. [48] demonstrated the sensitivity of their homemade SMM system to magnetism. They used a loop probe that differed from the usual probe and were able to observe an obvious contrast between ferromagnetic and paramagnetic materials that was both qualitative and quantitative. Their results are shown in Figure 9, where the maximum change in the FMR field is about  $230\ \text{Oe}$  in both images. As can be seen, a large amount of image smearing occurs near the edges of the sample.

**4.6. Imaging the Radiated Power of Microwave Chips.** In recent years, diagnosing problems within highly integrated microwave chips has received a lot of attention. The use of SMM to test chips offers opportunities for noncontact testing and a small scanning zone.

Lin et al. [49] have reported a resolution enhancement method for subsurface noninvasive application of imaging based on an SMM system that comprises an EMP (evanescent microwave probe), a VNA (vector network analyzer), a data capture system, and a motorized XYZ stage with high resolution. Thanks to the interferometric-based broadband matching architecture, adjustment of the sample–probe electromagnetic coupling is achievable so that the measurement can be highly sensitive at arbitrary frequencies between 2 and 18 GHz. The image processing approach uses the PSD (position/signal difference) and ARS (adaptive robust statistical) methods. Valid error rectification is possible with the proposed solution because of the measurement noise and specimen tilt so that the quality of imaging can be upgraded for the noninvasive assessment.

Kleismit et al. [50] tested a homemade  $\lambda/4$  evanescent microwave sensor. The sensor can be used for elucidating

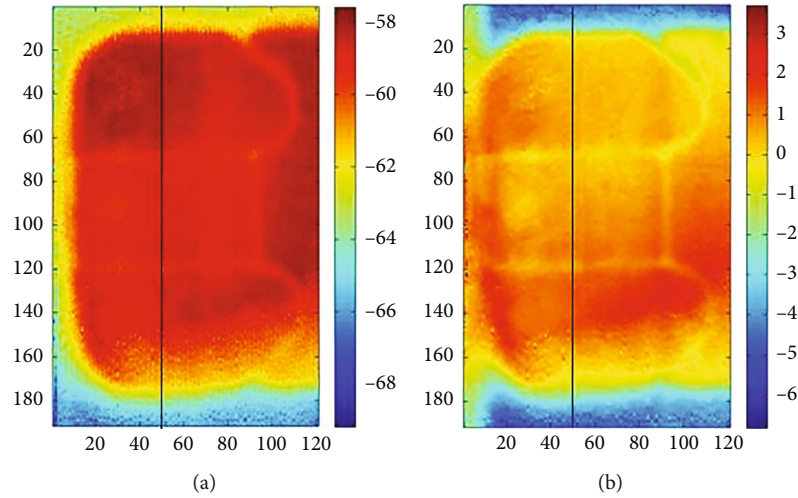


FIGURE 10: Application of the ARS method to case 3 ( $10\ \mu\text{m}$ - $80\ \mu\text{m}$ ) [49]. (a) Before the ARS processing. (b) After the ARS processing.

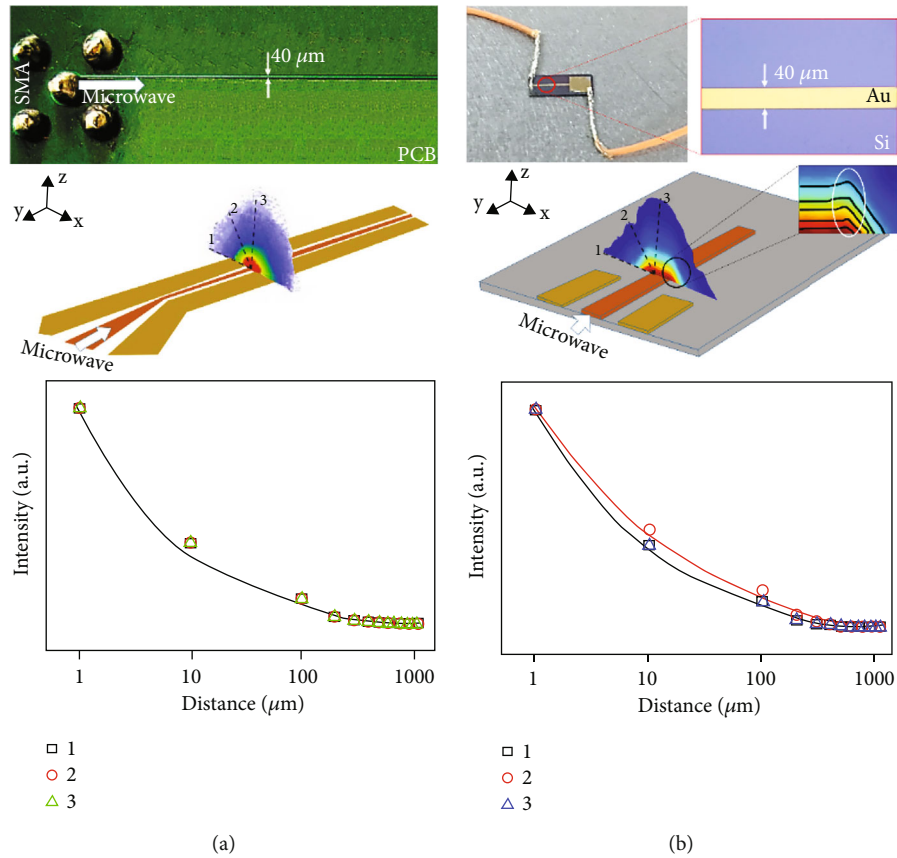


FIGURE 11: Spatial plots of the section of the bare copper wire and coplanar waveguide. (a) MW field distribution of the bare copper wire section and (b) MW field distribution of the CPW section [51].

the local electromagnetic properties of materials, as illustrated in Figure 10. The resonator intrinsic inherent spatial resolution of the resonator has been corroborated through experimental demonstration. The first-order approximation estimation of the sensitivity related to the sample-probe tip-sample interaction was presented for conductors, dielectrics, and superconductors. An estimation of the intrinsic sensitivity inherent to the resonant probe was also presented.

The sensitivity of the probe is in the range of micrometers. The system is also capable of generating the local complex permittivity values for dielectric, conductor, and superconductor sample specimens, which is achieved through the determination of the resonant frequency shift of the resonant coaxial probe toward the surface of the sample as the tip moves toward the sample surface. The resonant frequency shift is measured relative to the reference resonant

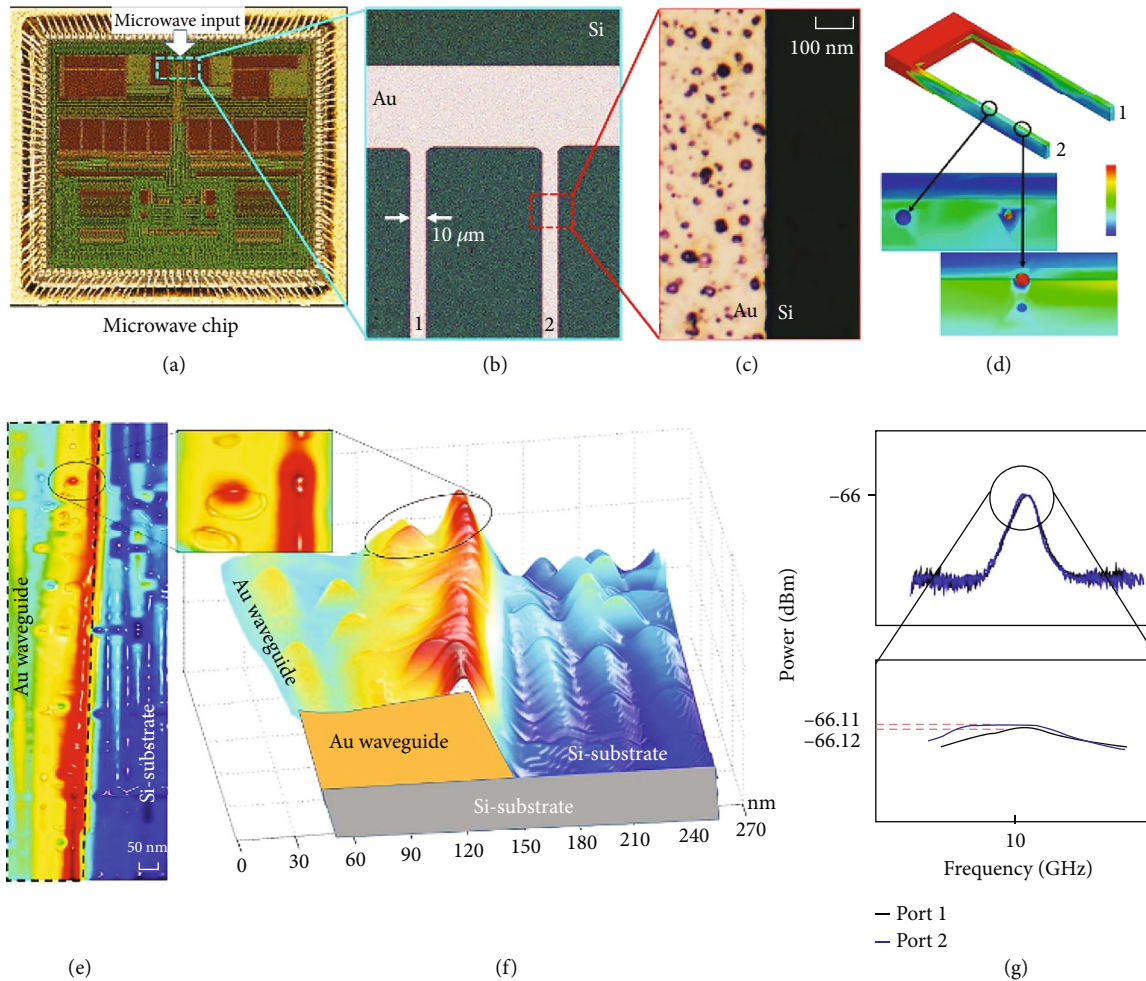


FIGURE 12: Spatial plots of the MW waveguide in the MW chip. (a) MW chip, (b) MW waveguide in the MW chip, (c) surface of the MW waveguide, (d) MW field simulation of the MW waveguide, (e) two-dimensional image of the MW field distribution in the MW waveguide, (f) the corresponding three-dimensional image of the MW field distribution in the MW waveguide, and (g) MW power in the two MW waveguides [51].

frequency, which is the resonance frequency when the tip is  $1\ \mu\text{m}$  from the surface.

**4.7. Imaging of Dynamic Microwave Fields.** The use of SMM offers a means of imaging the microwave field distribution when the chip is working in real-time. Guo et al. [51, 52] used a scanning microwave microscope with a microwave resonant cavity with a  $Q$  of 209 to identify nano defects on the waveguide surface in chips. They obtained microwave waveguide microwave field signals with a resolution of up to  $1\ \text{pW}$  and plotted the microwave field distribution in microwave core operation with a resolution that can reach  $15\ \text{nm}$ , as shown in Figures 11 and 12. This method offers high resolution and the capability for online monitoring for microwave chip evaluation and screening and, as such, could have far-reaching applications in chip fabrication, chip inspection, and nanostructure detection.

Chen et al. [52] proposed a simple method for testing very weak microwaves using a homemade scanning microwave microscope detection system consisting of a  $\lambda/4$  tun-

able resonant cavity and a tungsten tip. They solved the technical problem of impedance matching and inhibited the background noise by enhancing the number of cycles of the coupling loop. Using this approach, the efficiency of electromagnetic wave loading into the tip sampling system is improved, and the measured values of thermal parameters of the chip are obtained using a noncontact scanning mode.

**4.8. Imaging of Samples in Extreme Environments.** The demand for nondestructive testing in high-temperature environments has been increasing. Online or in-service high-temperature NDT systems will save time and energy, lower costs, and enhance efficiency [53].

Reznik and Yurasova [53] demonstrated the use of a homemade quartz lamp radiation module as a heater coupled to a homemade microwave microscope probe. They tested the amplitude and phase of a hexagonal honeycomb lattice at room temperature and  $50^\circ\text{C}$  at a resonant frequency of  $1\ \text{GHz}$ . Their work confirmed that multibands could be used for subsurface detection and superresolution imaging at high

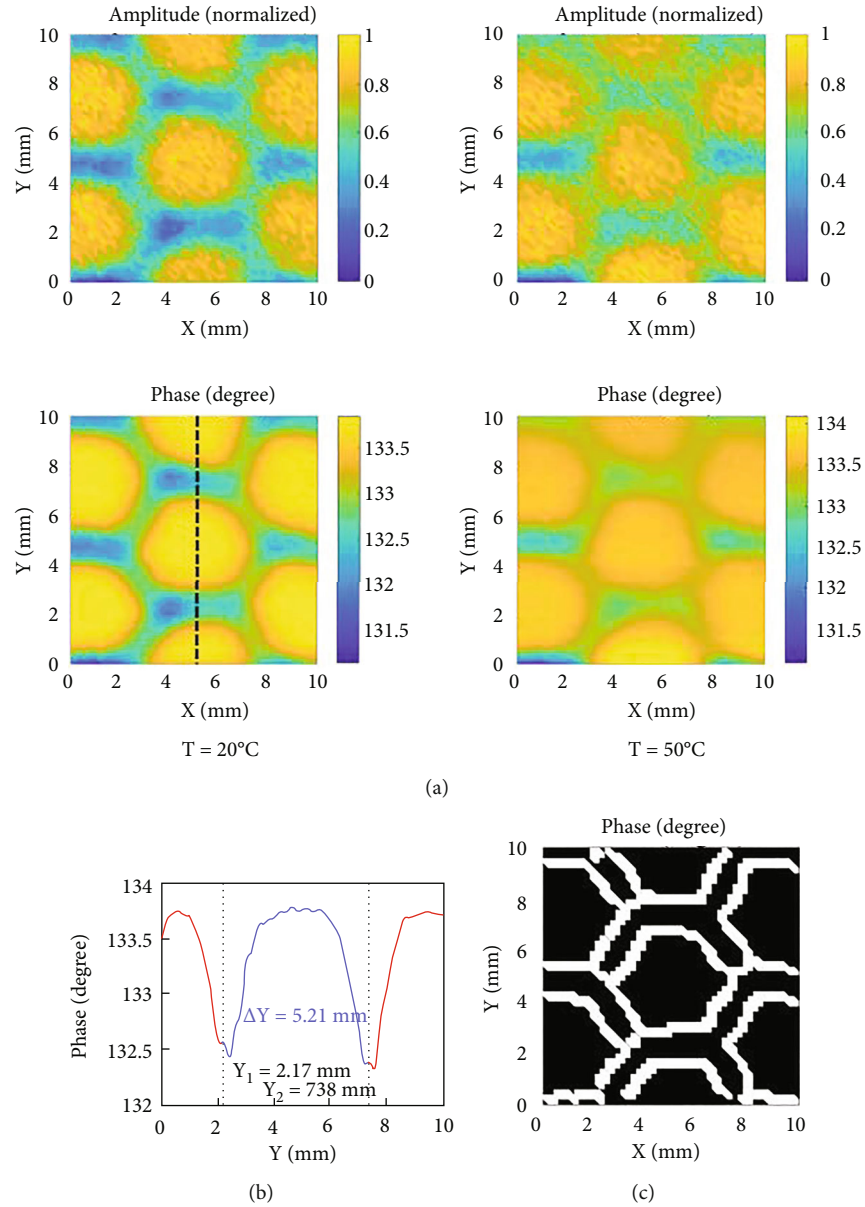


FIGURE 13: (a) Images of the scanning amplitude and phase of the inner honeycomb core at  $20^\circ\text{C}$  and  $50^\circ\text{C}$ , (b) the linear distribution of the phase, and (c) the phase image after edge detection processing [53].

temperatures. Their system could clearly distinguish metal gratings with line and gap widths of 0.5 mm at 1 GHz, and the resolution reached  $\lambda/600$  (Figure 13).

**4.9. Imaging of Biological Samples.** The attractiveness of microwave technology for biological applications stems from a combination of its sensitivity to water and dielectric contrasts and its noncontact and nondestructive nature [54].

Wu et al. [55] used a homemade scanning microwave microscope that allowed contact/tapping mode imaging of both nonconductive and conductive specimens [55]. Their system used a flexible CNT (carbon nanotube tip) carbon nanotube tip, which facilitated the upgrade in image quality and also protected the specimen surface from scratches. By manipulating the SMM and CNT tip in tapping mode, they

depicted the  $f_r$  and  $S_{11}$  amplitudes in a designated scan region and acquired photoresist stripes, gold-patterned numbers, and clear  $\text{B}_4\text{G}_{12}$  (corneal endothelial) cell images (Figure 14). In the acquired images, the cytoplasm and nucleus are distinguishable from the remaining part of the cell and peripheral medium, suggesting the possible SMM application in cellular imaging. This work lays the foundation for the further development and application of SMM techniques for soft matter imaging in biosciences. In Figures 14(c) and 14(d), the red area represents the nucleus, the yellow and green areas represent the outline of the cell, and the dark blue area corresponds to the cytoplasm, showing the quality of the image.

Farina et al. [56] presented a primitive interferometric procedure-based NFMM instrument for dielectric elucidation

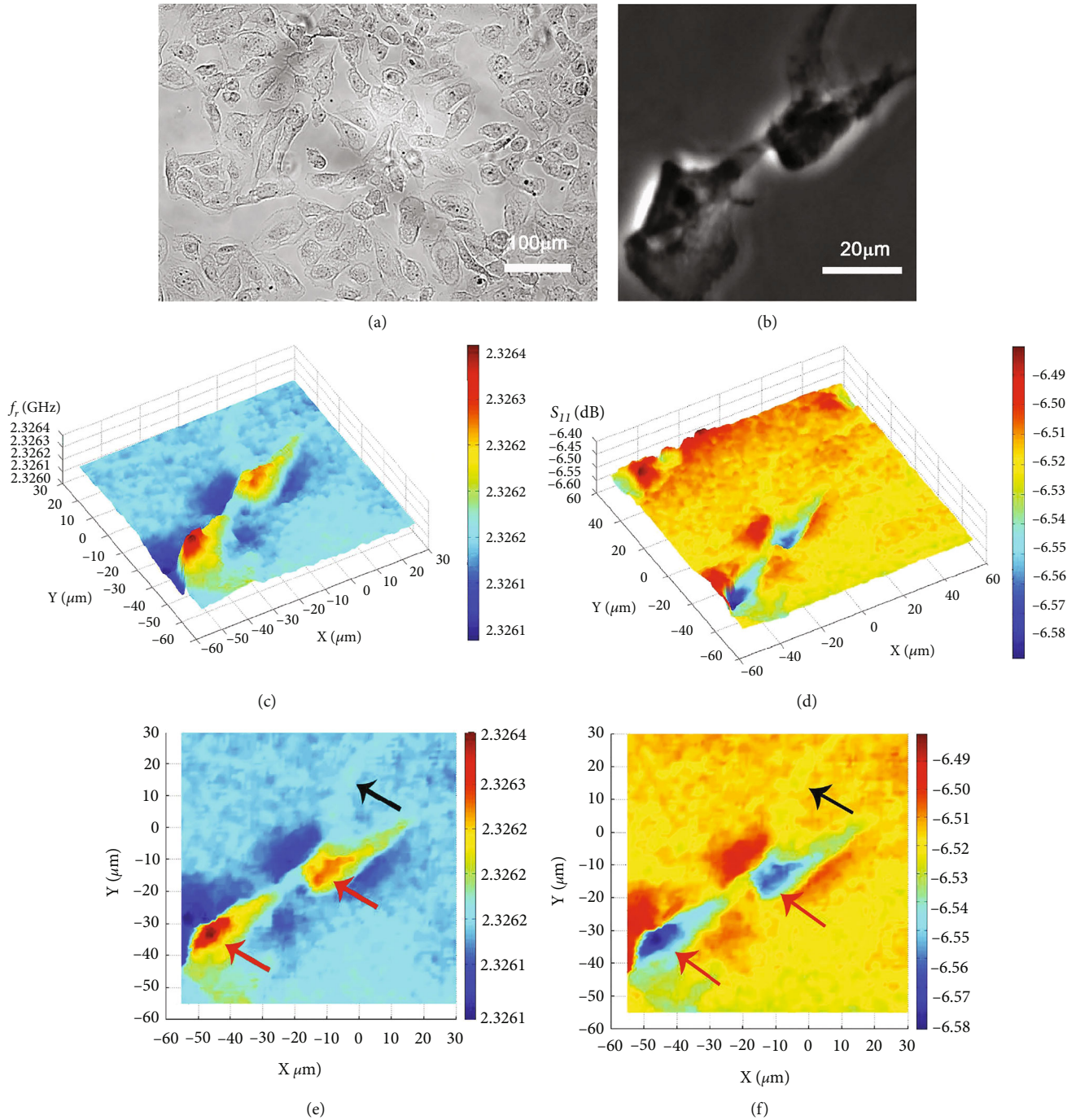


FIGURE 14: (a) The optical image of corneal endothelial cells ( $B_4G_{12}$ ) on a glass coverslip, (b) the phase contrast image of a pair of adjacent  $B_4G_{12}$  cells, (c) the resonant frequency  $f_r$  3D plot, (d)  $S_{11}$  amplitude 3D plot, (e) resonant frequency  $f_r$  contour plot, and (f)  $S_{11}$  amplitude contour plot [55].

in liquid media, where a vector network analyzer was integrated with an interferometric-based matching architecture and a novel fast microstrip probe that was prepared via a silicon deposition technique. This approach allowed a more-sensitive determination of microwave signals at the desired frequencies from 1 to 26 GHz. The system also had the virtue of simplicity.

Haddadi et al. [16] used SMM and scanning capacitance microscopy (SCM) to assess the presence of fullerene ( $C_{60}$ )

in dry cancer cell membranes after appropriate exposure. They analyzed the SMM data in the time and frequency domains. This preliminary study suggests that both SMM and SCM can be adopted to indicate the presence of  $C_{60}$  in cells, as shown in Figure 15. Fullerene is a nanoparticle being actively explored for possible uses in biology and medicine because of its lipophilic nature and ability to dope or permeate cell membranes.



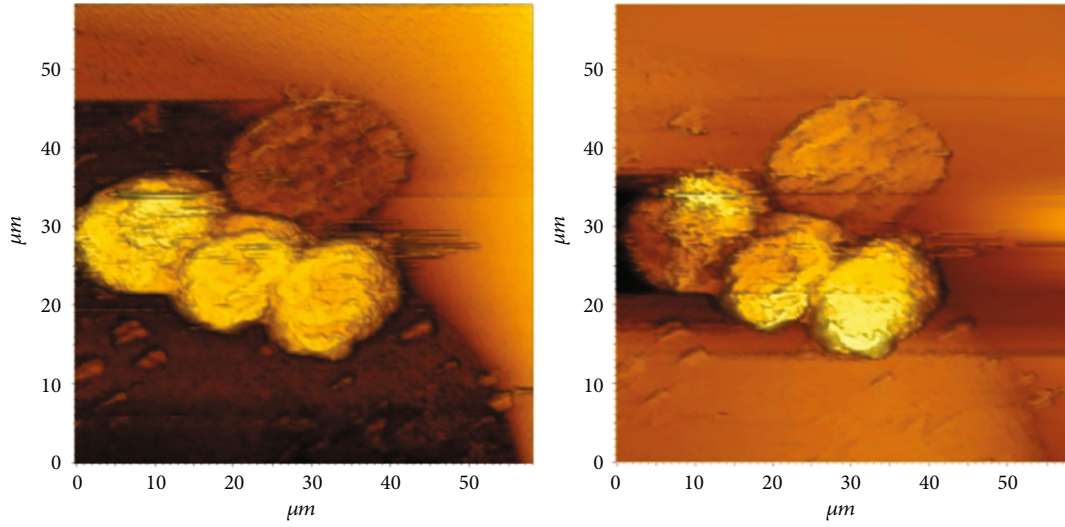


FIGURE 15: (a) Time-domain SMM image of MCF-7 cells treated with fullerene and (b) the simultaneous STM image (processed to remove the tilt plane). The taller cells are  $3 \mu\text{m}$  [16].

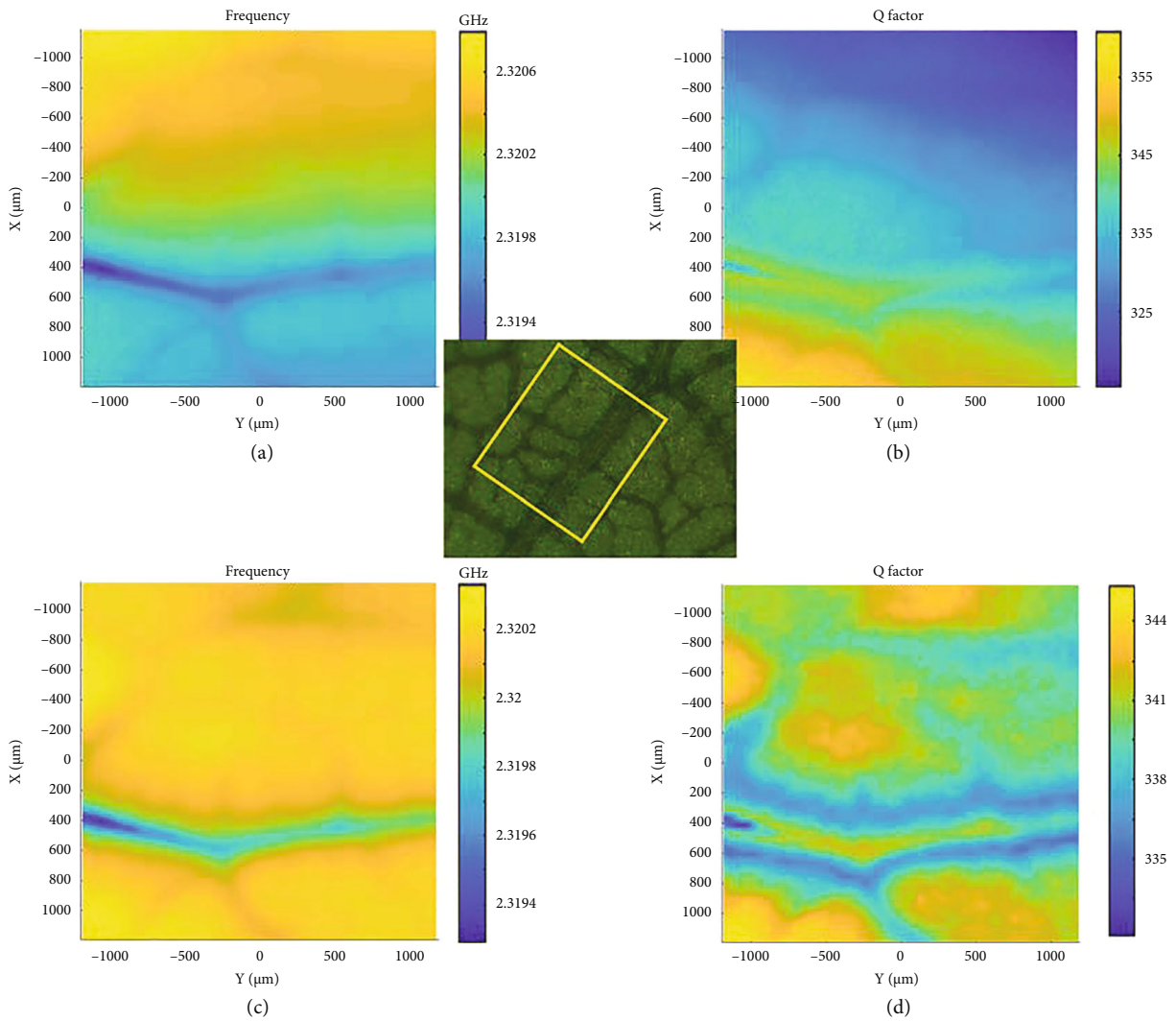


FIGURE 16: SMM image correction in the imaging of leaf veins. (a)  $f_r$  and (b) Q image of original data. (c) Tilt-corrected  $f_r$  image and (d) Q image [8].

Zhang et al. [8] reported a method that can correct the skewing and denoising of SMM images, significantly improving the spatial resolution of the images. They detected and obtained parametric images of  $f_r$ ,  $S_{11}$ , and  $Q$  of the veins of leaves, as illustrated in Figure 16. After the application of the tilt correction, the images were much clearer than the original blurred images.

## 5. Conclusions and Future Prospects

Scanning microwave microscopy has developed into a very broad research topic since its introduction and is favored by many researchers due to the nondestructive advantages of microwave testing [57–59]. It has now been successfully applied to characterize surface and subsurface samples at the nanoscale spatial resolution, exploring properties such as dielectric constant, doping concentration, and resistivity. In terms of the investigation of the electrical properties of materials, scanning microwave microscopy shows advantages over other conventional microscopies, being unaffected by temperature changes, the presence or absence of a vacuum, and can even work in strong magnetic field environments. It also has good prospects for the online detection of chip electromagnetic fields in real-time. However, there is still room for research in terms of microwave signal resolution and image optimization methods, and this is likely to prove a target for future exploration. At the same time, methods for transmitting microwaves more conducive to the tip radiation method are also being explored, such as the use of special AFM probes made of platinum [60] and micro- and nanoprocessing on silicon nitride cantilevers [61–63]. To improve the accuracy and sensitivity of microwave signal detection, we still need to both reduce the size of the probe under limited process conditions and reduce the influence of the noise signal on the test signal. We anticipate that the application scope of scanning microwave microscopy will continue to expand.

## Conflicts of Interest

The authors declare that there is no conflict of interest regarding the publication of this paper.

## Acknowledgments

This work was supported by the National Natural Foundation of China (NSFC) (61727804, 51727808, and 51922009), the Research Project Supported by Shanxi Scholarship Council of China (2021-117), and the Shanxi “1331 Project”.

## References

- [1] J. Gerber and M. Arcarese, “Non-destructive characterization of materials by evanescent microwaves,” *Measurement Science and Technology*, vol. 4, no. 5, pp. 583–590, 1993.
- [2] B. T. Rosner and D. W. V. D. Weide, “High-frequency near-field microscopy,” *Review of Scientific Instruments*, vol. 73, no. 7, pp. 2505–2525, 2002.
- [3] D. E. Steinhauer, C. P. Vlahacos, S. K. Dutta, B. J. Feenstra, F. C. Wellstood, and S. M. Anlage, “Quantitative imaging of sheet resistance with a scanning near-field microwave microscope,” *Applied Physics Letters*, vol. 72, no. 7, pp. 861–863, 1998.
- [4] M. Dressel and G. Grüner, *Electrodynamics of Solids*, Cambridge University Press, Illustrated edition, 2010.
- [5] S. M. Anlage, D. E. Steinhauer, B. J. Feenstra, C. P. Vlahacos, and F. C. Wellstood, “Near-Field Microwave Microscopy of Materials Properties,” in *Microwave Superconductivity*, Springer, Netherlands, 2001.
- [6] R. Zoughi, “Microwave non-destructive testing and evaluation,” *Non-Destructive Evaluation Series*, vol. 4, 2000.
- [7] G. Fabi, C. H. Joseph, E. Pavoni et al., “Real-Time Removal of Topographic Artifacts in Scanning Microwave Microscopy,” *IEEE Transactions on Microwave Theory and Techniques*, vol. 69, no. 5, pp. 2662–2672, 2021.
- [8] X. Zhang, Z. Wu, Q. Lan et al., “Improvement of spatial resolution by tilt correction in near-field scanning microwave microscopy,” *AIP Advances*, vol. 11, no. 3, article 035114, 2021.
- [9] N. Qaddoumi and R. Zoughi, “Microwave scattering characteristics of defective dielectric cylinders,” *Ndt & E International*, vol. 27, no. 6, pp. 299–305, 1994.
- [10] Y. G. Wang, M. E. Reeves, W. Chang, J. S. Horwitz, and W. Kim, “Near-Field imaging of the microwave dielectric properties of single-crystal  $\text{PbTiO}_3$  and thin-film  $\text{Sr}_{1-x}\text{BxTiO}_3$ ,” *MRS Proceedings*, vol. 603, 1999.
- [11] H. Bakli, K. Haddadi, and T. Lasri, “Interferometric technique for scanning near-field microwave microscopy applications,” *IEEE International Instrumentation & Measurement Technology Conference*, vol. 63, no. 5, pp. 1281–1286, 2013.
- [12] G. Dai, G. Geng, X. Zhang, J. Wang, T. Chang, and H. L. Cui, “W-band near-field microscope,” *IEEE Access*, vol. 7, pp. 48060–48067, 2019.
- [13] G. Fabi, X. Jin, E. Pavoni et al., “Quantitative characterization of platinum diselenide electrical conductivity with an inverted scanning microwave microscope,” *IEEE Transactions on Microwave Theory and Techniques*, vol. 69, no. 7, pp. 3348–3359, 2021.
- [14] K. Karrat, R. D. Grober, and M. A. Paesler, “Tip-sample distance control for near-field scanning optical microscopes,” *Proceedings of SPIE - The International Society for Optical Engineering*, vol. 2535, pp. 1842–1844, 1995.
- [15] A. P. Gregory, J. F. Blackburn, K. Lees et al., “Measurement of the permittivity and loss of high-loss materials using a near-field scanning microwave microscope,” *Ultramicroscopy*, vol. 161, pp. 137–145, 2016.
- [16] K. Haddadi, J. Marzouk, S. Gu, S. Arscott, G. Dambrine, and T. Lasri, “Interferometric near-field microwave microscopy platform for electromagnetic micro-analysis,” *Procedia Engineering*, vol. 87, pp. 388–391, 2014.
- [17] M. Farina, A. D. Donato, D. Mencarelli, G. Venanzoni, and A. Morini, “High resolution scanning microwave microscopy for applications in liquid environment,” *IEEE Microwave & Wireless Components Letters*, vol. 22, no. 11, pp. 595–597, 2012.
- [18] M. Golosovsky and D. Davidov, “Novel millimeter-wave near-field resistivity microscope,” *Applied Physics Letters*, vol. 68, no. 11, pp. 1579–1581, 1996.
- [19] J. Lee, C. J. Long, H. Yang, X. D. Xiang, and I. Takeuchi, “Atomic resolution imaging at 2.5 GHz using near-field microwave microscopy,” *Applied Physics Letters*, vol. 97, no. 18, p. 183111, 2010.

- [20] C. Gao, T. Wei, F. Duewer, Y. Lu, and X. D. Xiang, "High spatial resolution quantitative microwave impedance microscopy by a scanning tip microwave near-field microscope," *Applied Physics Letters*, vol. 71, no. 13, pp. 1872–1874, 1997.
- [21] D. E. Steinhauer, C. P. Vlahacos, S. K. Dutta, F. C. Wellstood, and S. M. Anlage, "Surface resistance imaging with a scanning near-field microwave microscope," *Applied Physics Letters*, vol. 71, no. 12, pp. 1736–1738, 1997.
- [22] S. M. Anlage, V. V. Talanov, and A. R. Schwartz, "Principles of near-field microwave microscopy," *Scanning Probe Microscopy*, vol. 1, pp. 207–245, 2007.
- [23] G. Vlachogiannakis, H. T. Shivamurthy, M. Pino, and M. Spirito, "An I/Q-mixer-steering interferometric technique for high-sensitivity measurement of extreme impedances," in *2015 IEEE MTT-S International Microwave Symposium*, Phoenix, AZ, USA, 2015.
- [24] S. Ramo, J. R. Whinnery, and T. V. Duzer, *Fields and Waves in Communication Electronics*, Wiley, 1994.
- [25] A. S. Thanawalla, S. K. Dutta, C. P. Vlahacos et al., "Microwave near-field imaging of electric fields in a superconducting microstrip resonator," *Applied Physics Letters*, vol. 73, no. 17, pp. 2491–2493, 1998.
- [26] C. C. Williams, W. P. Hough, and S. A. Rishton, "Scanning capacitance microscopy on a 25 nm scale," *Applied Physics Letters*, vol. 55, no. 2, pp. 203–205, 1989.
- [27] Y. Manassen, R. J. Hamers, J. E. Demuth, and A. J. Castellano Jr, "Direct observation of the precession of individual paramagnetic spins on oxidized silicon surfaces," *Physical Review Letters*, vol. 62, no. 21, pp. 2531–2534, 1989.
- [28] S. Fabiani, D. Mencarelli, A. Di Donato et al., "Broadband Scanning Microwave Microscopy Investigation of Graphene," in *2011 IEEE MTT-S International Microwave Symposium*, Baltimore, MD, USA, 2011.
- [29] J. Kim, M. S. Kim, K. Lee, J. Lee, D. Cha, and B. Friedman, "Development of a near-field scanning microwave microscope using a tunable resonance cavity for high resolution," *Measurement Science and Technology*, vol. 14, no. 1, pp. 7–12, 2003.
- [30] K. A. Bertness, J. B. Schlager, N. A. Sanford et al., "Application of microwave scanning probes to photovoltaic materials," in *2010 35th IEEE Photovoltaic Specialists Conference*, Honolulu, HI, USA, 2010.
- [31] V. V. Talanov, A. Scherz, R. L. Moreland, and A. R. Schwartz, "A near-field scanning microwave probe for spatially localized electrical metrology," *Applied Physics Letters*, vol. 88, no. 13, article 114701, 2006.
- [32] M. Tabib-Azar, P. S. Pathak, G. Ponchak, and S. LeClair, "Nondestructive superresolution imaging of defects and non-uniformities in metals, semiconductors, dielectrics, composites, and plants using evanescent microwaves," *Review of Scientific Instruments*, vol. 70, no. 6, pp. 2783–2792, 1999.
- [33] M. Fecioru-Morariu, S. R. Ali, C. Papusoi, M. Sperlich, and G. Güntherodt, "Effects of Cu dilution in IrMn on the exchange bias of CoFe/IrMn bilayers," *Physical Review Letters*, vol. 99, no. 9, article 097206, 2007.
- [34] Z. Wu, A. D. Souza, B. Peng, W. Q. Sun, S. Y. Xu, and C. K. Ong, "Measurement of high frequency conductivity of oxide-doped anti-ferromagnetic thin film with a near-field scanning microwave microscope," *AIP Advances*, vol. 4, no. 4, article 47114, 2014.
- [35] A. Imtiaz, T. Baldwin, H. T. Nembach, T. M. Wallis, and P. Kabos, "Near-field microwave microscope measurements to characterize bulk material properties," *Applied Physics Letters*, vol. 90, no. 24, pp. 243105–243253, 2007.
- [36] R. King, M. Owens, and T. W. Tai, "The propagation of lateral electromagnetic waves in air over vertical discontinuities," in *Lateral Electromagnetic Waves*, Springer, New York, NY, 1992.
- [37] J. R. Wait, "Impedance characteristics of electric dipoles over a conducting half-space," *Radio Science*, vol. 4, no. 10, pp. 971–975, 1969.
- [38] A. Tselev, S. M. Anlage, Z. Ma, and J. Melngailis, "Broadband dielectric microwave microscopy on micron length scales," *The Review of Scientific Instruments*, vol. 78, no. 4, p. 044701, 2007.
- [39] B. A. Bagdad, C. Lozano, and F. Gamiz, "Near-field scanning microwave microscope platform based on a coaxial cavity resonator for the characterization of semiconductor structures," *Solid-State Electronics*, vol. 159, pp. 150–156, 2019.
- [40] C. Gao and X. D. Xiang, "Quantitative microwave near-field microscopy of dielectric properties," *Review of Scientific Instruments*, vol. 69, no. 11, pp. 3846–3851, 1998.
- [41] A. P. Gregory, J. F. Blackburn, K. Lees et al., "A near-field scanning microwave microscope for measurement of the permittivity and loss of high-loss materials," in *84th ARFTG Microwave Measurement Conference*, Boulder, CO, USA, 2015.
- [42] F. L. Pearanda-Foix, "Detection of anti-counterfeiting markers through permittivity maps using a micrometer scale near field scanning microwave microscope," *Sensors*, vol. 21, no. 16, p. 5463, 2021.
- [43] K. Matsuba, S. Yoshizawa, Y. Mochizuki, T. Mochiku, K. Hirata, and N. Nishida, "Anti-phase modulation of electron- and hole-like states in vortex core of Bi2Sr2CaCu2Ox probed by scanning tunneling spectroscopy," *Journal of the Physical Society of Japan*, vol. 76, no. 6, pp. 1321–1339, 2007.
- [44] Y. Niimi, T. Matsui, H. Kambara, K. Tagami, M. Tsukada, and H. Fukuyama, "Scanning tunneling microscopy and spectroscopy of the electronic local density of states of graphite surfaces near monoatomic step edges," *Physical Review B, Condensed Matter*, vol. 73, no. 8, 2006.
- [45] T. Machida, M. B. Gaifullin, S. Ooi, T. Kato, H. Sakata, and K. Hirata, "Local measurement of microwave response with local tunneling spectra using near field microwave microscopy," *Applied Physics Express*, vol. 2, no. 2, article 25006, 2009.
- [46] I. Lee, Y. Obukhov, G. Xiang et al., "Nanoscale scanning probe ferromagnetic resonance imaging using localized modes," *Nature*, vol. 466, no. 7308, pp. 845–848, 2010.
- [47] I. Lee, R. Adur, C. Hamann et al., "Scanning probe ferromagnetic resonance imaging of stripe patterned exchange bias IrMn-NiFe film using nanoscale confined modes," *APS Meeting Abstracts*, vol. 2011, 2011.
- [48] S. C. Lee, C. P. Vlahacos, B. J. Feenstra et al., "Magnetic permeability imaging of metals with a scanning near-field microwave microscope," *Applied Physics Letters*, vol. 77, no. 26, pp. 4404–4406, 2000.
- [49] T. Lin, S. Gu, and T. Lasri, "Resolution improvement method for non-destructive imaging with near-field scanning microwave microscopy," in *2018 48th European Microwave Conference (EuMC)*, Madrid, Spain, 2018.
- [50] R. A. Kleismit, M. K. Kazimierczuk, and G. Kozlowski, "Sensitivity and resolution of evanescent microwave microscope," *IEEE Transactions on Microwave Theory and Techniques*, vol. 54, no. 2, pp. 639–647, 2006.

- [51] H. Guo, X. Li, Q. Zhu et al., "Imaging nano-defects of metal waveguides using the microwave cavity interference enhancement method," *Nanotechnology*, vol. 31, no. 45, article 455203, 2020.
- [52] C. Yulei, Z. Zhang, Q. Zhu et al., "A weak microwave detection method based on resonator noise suppression technology," *Japanese Journal of Applied Physics*, vol. 59, no. 4, article 040903, 2020.
- [53] W. Peiyu, L. Zhencheng, and P. Yongmao, "In situ high temperature microwave microscope for nondestructive detection of surface and sub-surface defects," *Optics Express*, vol. 26, no. 8, 2018.
- [54] A. N. Reznik and N. V. Yurasova, "Near-field microwave tomography of biological objects," *Technical Physics*, vol. 49, no. 4, pp. 485–493, 2004.
- [55] Z. Wu, W. Q. Sun, T. Feng et al., "Imaging of soft material with carbon nanotube tip using near-field scanning microwave microscopy," *Ultramicroscopy*, vol. 148, pp. 75–80, 2015.
- [56] M. Farina, F. Piacenza, F. De Angelis et al., "Broadband near-field scanning microwave microscopy investigation of fullerene exposure of breast cancer cells," in *2016 IEEE MTT-S International Microwave Symposium (IMS)*, San Francisco, CA, USA, 2016.
- [57] A. Imtiaz and S. Anlage, "A novel scanning near-field microwave microscope capable of high resolution loss imaging," *APS Meeting Abstracts*, vol. 2004, 2004.
- [58] A. Imtiaz, M. Pollak, S. M. Anlage, J. D. Barry, and J. Melngailis, "Near-Field Microwave Microscopy on Nanometer Length Scales," *Journal of Applied Physics*, vol. 97, no. 4, 2005.
- [59] A. Lucibello, G. M. Sardi, G. Capoccia et al., "A broadband toolbox for scanning microwave microscopy transmission measurements," *Review of Scientific Instruments*, vol. 87, no. 5, article 053110, 2016.
- [60] C. H. Joseph, G. M. Sardi, S. S. Tuca et al., "Scanning microwave microscopy technique for nanoscale characterization of magnetic materials," *Journal of Magnetism & Magnetic Materials*, vol. 420, pp. 62–69, 2016.
- [61] K. Lai, M. B. Ji, N. Leindecker, M. A. Kelly, and Z. X. Shen, "Atomic-force-microscope-compatible near-field scanning microwave microscope with separated excitation and sensing probes," *Review of Scientific Instruments*, vol. 78, no. 6, article 063702, 2007.
- [62] K. Lai, W. Kundhikanjana, M. Kelly, and Z. X. Shen, "Modeling and characterization of a cantilever-based near-field scanning microwave impedance microscope," *Review of Scientific Instruments*, vol. 79, no. 6, article 063703, 2008.
- [63] P. F. Medina, A. Lucibello, G. Gramse et al., "Transmission and reflection mode scanning microwave microscopy (SMM): experiments, calibration, and simulations," in *2015 European Microwave Conference (EuMC)*, Paris, France, 2015.

## Research Article

# Raman Spectroscopy-Assisted Characterization of Nanoform MoS<sub>2</sub> Thin Film Transistor

Rajasekaran Saminathan <sup>1</sup>, Haitham Hadidi,<sup>1</sup> Mohammed Tharwan <sup>1</sup>, Ali Alnujaie,<sup>1</sup>  
Jabril A. Khamaj,<sup>1</sup> and Gunasekaran Venugopal <sup>2</sup>

<sup>1</sup>Mechanical Engineering Department, Faculty of Engineering, Jazan University, P. O. Box 45142, Jazan, Saudi Arabia

<sup>2</sup>Department of Materials Science, School of Technology, Central University of Tamil Nadu, Thiruvavur, 610005 Tamil Nadu, India

Correspondence should be addressed to Gunasekaran Venugopal; [gunasekaran@cutn.ac.in](mailto:gunasekaran@cutn.ac.in)

Received 16 January 2022; Revised 22 May 2022; Accepted 30 May 2022; Published 22 June 2022

Academic Editor: Zhichao Lou

Copyright © 2022 Rajasekaran Saminathan et al. This is an open access article distributed under the Creative Commons Attribution License, which permits unrestricted use, distribution, and reproduction in any medium, provided the original work is properly cited.

In this paper, we report the simple preparation and investigation of electrical transport properties of nanoform MoS<sub>2</sub> thin film transistor (TFT) devices. MoS<sub>2</sub> nanoparticles were synthesized by using the hydrothermal method. The physiochemical characterizations such as UV-vis, Fourier transform infrared, X-ray diffraction, and Raman spectroscopy studies were performed. Spin-coating was used to make the thin film on which silver electrodes were made. We observed nonlinear current-voltage (I-V) characteristics; however, the symmetricity was found in the I-V curve which confirms the no formation of the Schottky barrier between thin film and electrodes. Transistor transfer characteristics reveal that the TFT device is n-doped as more drain current modulation is observed when the positive gate voltage is applied. The relationship between gate-current and gate voltage studies concludes that there is no leakage gate current in the TFT device which further confirms the good reliability of transfer characteristics of a device. The device mobility was calculated as  $\sim 10.2 \text{ cm}^2/\text{Vs}$ , and the same was explained with plausible reason supported with Raman spectra analysis.

## 1. Introduction

Presently, two-dimensional materials (graphene, graphene-oxide, MoS<sub>2</sub>, and Bi<sub>2</sub>Se<sub>3</sub>) have been known for their unique characteristics and having potential prospects in various fields such as electronics, photovoltaic, sensors, flexible displays, supercapacitors, and water purification [1, 2]. Transition metal dichalcogenide semiconductors (TMDC) have significantly attracted the scientific community because of their unique electrical and optical characteristics. Molybdenum disulfide (MoS<sub>2</sub>) is a layered structure transition metal dichalcogenide material with weak van der Waals interlayer force, which is considered as a best candidate material for numerous applications such as supercapacitor, hydrogen generation/storage, photocatalyst, and rechargeable batteries [3–8]. MoS<sub>2</sub> has a hexagonal atomic arrangement similar to graphene. Mo and S atoms are stacked together in a single lattice and the weak van der Waals forces exist between the

interlayers. Monolayer or bulk MoS<sub>2</sub> may have different functions due to bandgap. It has been reported that the bulk MoS<sub>2</sub> having an indirect bandgap of 1.29 eV and monolayer MoS<sub>2</sub> having a direct bandgap of 1.9 eV [9] exist in a few forms of crystal structures such as 1T-MoS<sub>2</sub> (tetragonal), 2H-MoS<sub>2</sub> (hexagonal), and 3R-MoS<sub>2</sub> (rhombohedral) [10]. As per the report by Radisavljevic et al., the pristine single crystal-based MoS<sub>2</sub> field effect transistors have shown mobility of  $200 \text{ cm}^2/\text{Vs}$  with a current on/off ratio of  $10^8$  [11]. Particularly, MoS<sub>2</sub> received special attention among the TMDCs and believed as an alternative material for graphene (which has zero bandgap) in electronics [12].

By having salient features such as nominal bandgap, good carrier mobility, and interesting geometry, MoS<sub>2</sub> rises as an important candidate material in electronics and transistor development [13]. MoS<sub>2</sub> thin films have shown tremendous potentiality in the applications such as nanogenerators, electrochemical supercapacitors, photovoltaic cells, sensors,

and detectors [14–16]. The thermal instability of nanomaterials is the unavoidable parameter for these devices, because the materials may be heated due to photon absorption, charge carrier flow, and surrounding environment which may affect the device performance. Substrate used for material deposition also plays a key role in thermal stability. Previously, it was reported that monolayer thin film on SiO<sub>2</sub> substrate is thermally stable compared to bulk MoS<sub>2</sub>. However, the preparation of large area thin film with a uniform surface is still a quite difficult process and suitable appropriate methods have to be followed. Some reports were published recently on the large area thin films which were made using physical vapor deposition (PVD), chemical vapor deposition (CVD), vapor epitaxy, pulsed-laser depositor (PLD) and sputtering methods [14, 17]. These methods involve high costs and large manpower with complicated process procedures. Hence, a simple and cost-effective method is required as an alternative. In this work, we used a hydrothermal method to produce MoS<sub>2</sub> nanoparticles and used spin-coating to make large area thin film. The hydrothermal method is a simple and cost-effective method through which good quality samples can be prepared and large area thin films can be formed by spin-coating with thickness control by standardizing the film-making procedures [18, 19].

In the recent past, only a few studies have been reported on the electrical transport properties of MoS<sub>2</sub> thin film transistors (TFT) [20, 21], and their electronic transport properties and their mechanism are not explored well and required to be investigated more. Hence in this paper, we report the simple preparation procedure of MoS<sub>2</sub> nanoparticles, thin film making, and the electrical transport characteristics of MoS<sub>2</sub> TFT in detail.

## 2. Materials and Methods

**2.1. Materials.** All the research grade materials such as molybdenum oxide (MoO<sub>3</sub>), potassium thiocyanate, HCl (35 wt%), ethanol, and NaOH were purchased from Sigma-Aldrich and used without further purification. Deionized water is used in all experiments.

**2.2. Preparation of MoS<sub>2</sub> Samples.** MoS<sub>2</sub> nanoparticles were prepared by using the hydrothermal method [18, 22] using molybdenum oxide (MoO<sub>3</sub>) and potassium thiocyanate as precursor starting materials. Initially, 0.3 g of MoO<sub>3</sub> (1.5 mmol) and 0.5 g of potassium thiocyanate (4 mmol) were dissolved in 50 mL of deionized water and the same was sonicated for 1 hr. Then, HCl solution (1 mol/L) was added in order to keep the solution pH value to 2.0, and the solution has been stirred for another 45 min. Thereafter, the solution has been transferred into a stainless-steel autoclave (Teflon-lined, 100 mL capacity) for the hydrothermal treatment at 250°C for 40 hrs. After the treatment, the system is allowed to be cooled to room temperature. Then, the centrifugation is done with 5000 rpm for 20 min resulting black colored MoS<sub>2</sub> particles which were washed several times using ethanol and DI water. Then, the sample has been put inside a vacuum oven at 70°C (10 hrs) for drying. Spin-

coating is used to prepare MoS<sub>2</sub> thin film and silver paste was used to make contact electrodes.

**2.3. Instrumentation.** The absorption spectra of MoS<sub>2</sub> nanoparticles were taken using the UV-vis spectrophotometer (model: Jasco V-670). Fourier transform infrared spectroscopy (FT-IR) was performed via FT spectrometer (model: Nicolet-6700, USA). Further, MoS<sub>2</sub> thin film was analyzed with X-ray diffractometer (model: Shimadzu, XRD 6000) with Cu-K<sub>α</sub> radiation from the range of 10–70. Raman studies were done in Raman spectrometer (model: Horiba Scientific, LABRAM). All the electrical transport analyses have been performed using the semiconductor parameter analyzer (model: Agilent, B1500A).

## 3. Results and Discussion

Surface morphology of MoS<sub>2</sub> thin film has been studied by using scanning electron microscopy (SEM), transmission electron microscopy (TEM), and atomic force microscopy (AFM) techniques.

In Figure 1(a), the SEM image of MoS<sub>2</sub> thin film is shown which clearly shows an irregular surface morphology of MoS<sub>2</sub> thin film with wrinkled-like morphology. In Figure 1(b), the TEM image of MoS<sub>2</sub> is shown which clearly depicts the sheet-like morphology with transparent nature. The 2D topography of MoS<sub>2</sub> thin film was studied by using AFM (which is shown in Figure 1(c)) which shows an average surface roughness of MoS<sub>2</sub> thin film with value of 64 nm. This roughness is due to the overlapping of many MoS<sub>2</sub> platelets so that the measured region might consist of overlapped MoS<sub>2</sub> layers.

The optical image of MoS<sub>2</sub> thin film is shown in Figure 2(a). The UV-vis spectroscopy graph as shown in Figure 2(b) reveals the absorption spectra at 208 nm. The peak observed in the near UV region is mainly caused by the excitonic characteristics of MoS<sub>2</sub> nanoparticles [23]. In order to study the chemical compositions and vibration bonds in the sample, FT-IR measurement has been done which is shown in Figure 2(c). There is a feeble absorption peak at near 470 cm<sup>-1</sup> which is ascribed to the characteristics Mo-S vibration mode and well-matched with the previous report [24].

The XRD pattern of the MoS<sub>2</sub> thin film is shown in Figure 2(d). The main characteristic diffraction peak observed at 14.5° represents the (002) plane of the hexagonal structure of MoS<sub>2</sub> and matched with the previous report [25]. Moreover, the other diffraction peaks were observed at 33°, 40°, 44°, 50°, and 61° representing the (100), (103), (005), (105), and (008) crystal planes of MoS<sub>2</sub>, respectively. This XRD data shows a good agreement with JCPDS card no. 37-1492.

### 3.1. Electrical Transport Studies

**3.1.1. Current-Voltage (I-V) Characterization of MoS<sub>2</sub> Thin Film.** The current-voltage characteristics of MoS<sub>2</sub> thin film is shown in Figure 3(a).

It shows a slight nonlinear behavior. However, a clear symmetricity has been seen in I-V curve shown in

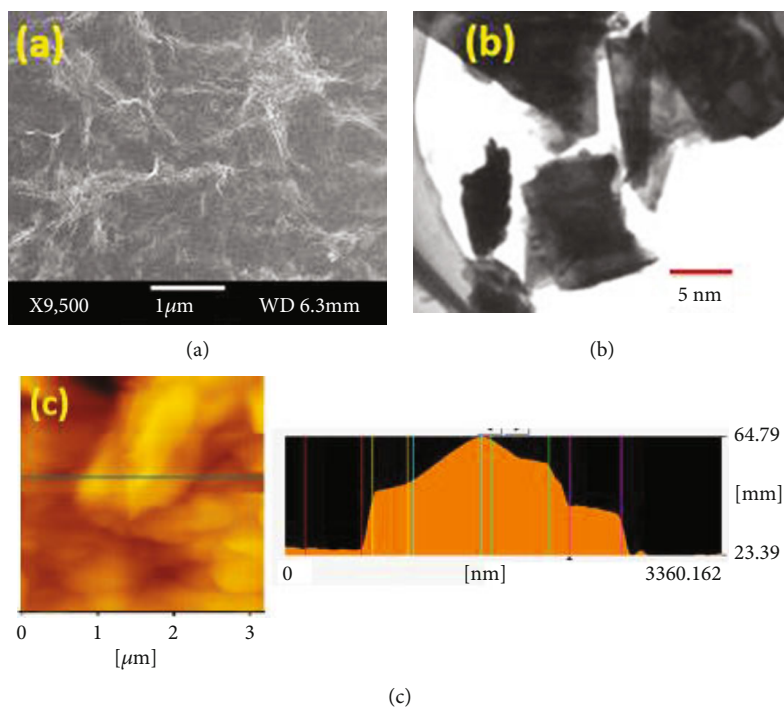


FIGURE 1: (a) SEM image of MoS<sub>2</sub> thin film. (b) TEM image of MoS<sub>2</sub> nanofilm. (c) AFM image of MoS<sub>2</sub> thin film, showing the thickness profile of 64 nm.

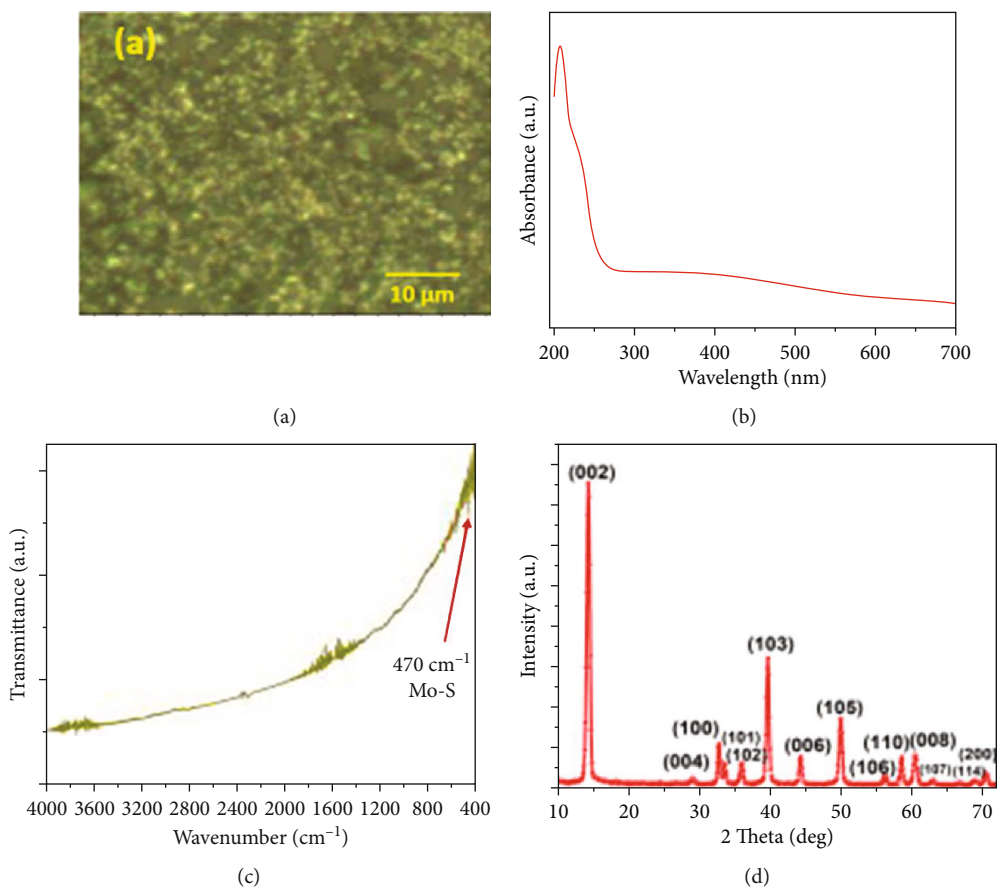


FIGURE 2: (a) Optical photograph of MoS<sub>2</sub> thin film. (b) UV-vis spectra of MoS<sub>2</sub> nanoparticles. (c) FT-IR spectra of MoS<sub>2</sub> nanoparticles. (d) XRD spectra of MoS<sub>2</sub> thin film.

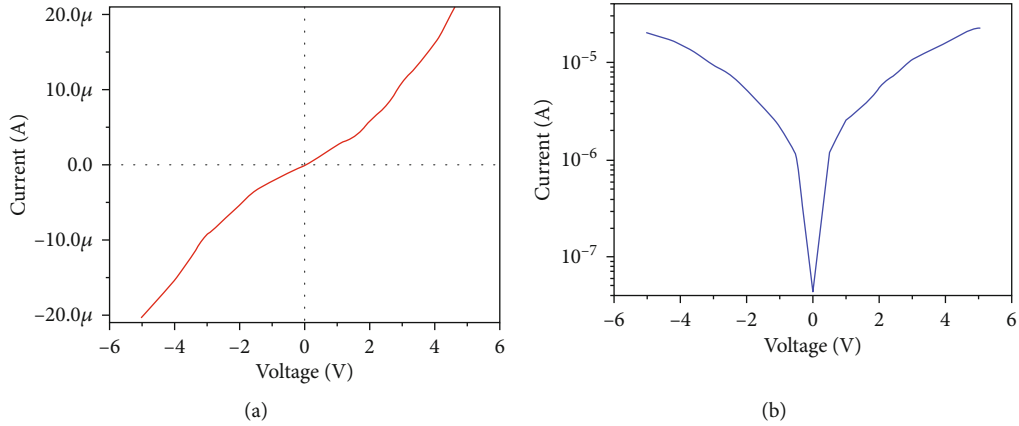


FIGURE 3: (a) Current-voltage characteristics of MoS<sub>2</sub> thin film. (b) Semilog I-V plot reveals a clear symmetry.

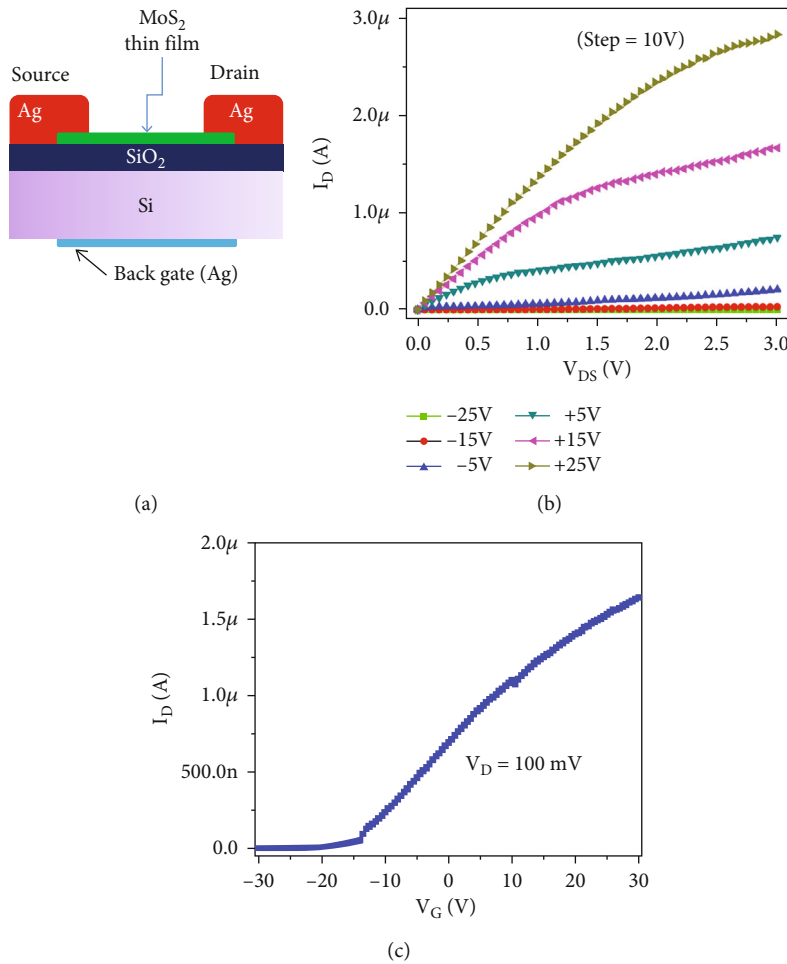


FIGURE 4: (a) The schematic of the MoS<sub>2</sub> TFT device. (b) Output characteristics ( $I_D$  versus  $V_{DS}$ ) of MoS<sub>2</sub> TFT device at different back gate voltages. An apparent linear ohmic behavior is observed. (c) Transfer characteristics ( $I_D$ - $V_G$ ) of the same device.

Figure 3(b) which further confirms the no formation of the Schottky barrier between the contacts and thin film.

**3.1.2. Characterization of MoS<sub>2</sub> Thin Film Transistor (TFT).** The schematic of the fabricated MoS<sub>2</sub> TFT device is shown in Figure 4(a).

The transistor characteristics are studied for MoS<sub>2</sub> thin film and their output characteristics ( $I_D$ - $V_{DS}$ ) for the different back-gate voltages ( $V_G$ ) varying from -25 to 25 V with a step of 10 V are shown in Figure 4(b). We observed a linear  $I_D$  versus  $V_{DS}$  curve, confirming an ohmic contact between thin film and electrodes. The transfer characteristics ( $I_D$ -



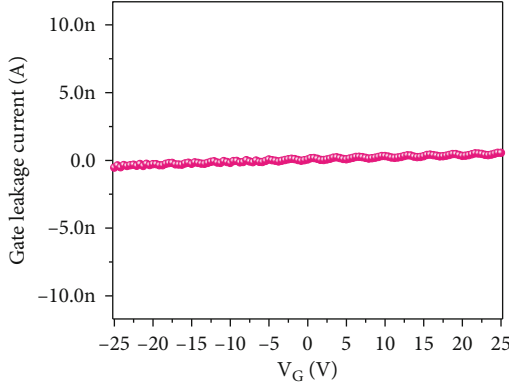


FIGURE 5: Gate leakage current versus gate bias voltage characteristics of MoS<sub>2</sub> TFT.

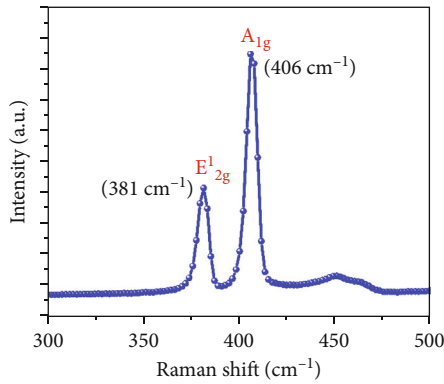


FIGURE 6: Raman spectra of MoS<sub>2</sub> thin film.

$V_G$ ) of MoS<sub>2</sub> TFT are shown in Figure 4(c), where the applied bias voltage is 100 mV.

When the gate voltage is increased, the drain current is also increased, which reveals the n-type behavior of TFT. Positive gate voltage produces more drain-current modulation than negative gate voltage ( $V_G$ ). The appearance of the charge neutrality point ( $V_{CNP}$ ) at the negative bias region ( $V_G \sim -20$  V) further concludes that the TFT device is n-doped. Figure 5 shows the relationship between gate current (IG) and gate voltage ( $V_G$ ).

This shows the negligible gate current through the SiO<sub>2</sub> oxide layer and confirms the excellent reliability of transfer characteristics presented in Figure 4(b). In addition, we extracted the mobility of our fabricated TFT device. The mobility ( $\mu$ ) of MoS<sub>2</sub> TFT was calculated using the following.

$$\mu = \frac{L \times g_m}{W \times C_{ox} \times V_d}, \quad (1)$$

where channel length ( $L$ ) is equal to 30  $\mu$ m, the channel width ( $W$ ) is equal to 25  $\mu$ m, and the capacitance between the channel and back gate per unit area is  $C_{ox}$  where  $C_{ox} = \xi_0 \xi_r / d = 3.83 \times 10^{-8}$  F/m<sup>2</sup>, where  $\xi_0$  is the permittivity of free space,  $\xi_r$  is 3.9 for SiO<sub>2</sub>, and  $d$  is gate oxide thickness

(90 nm). We determined the mobility of MoS<sub>2</sub> TFT as  $\sim 10.2$  cm<sup>2</sup>/Vs from these data. This is comparable to the mobility of multilayer MoS<sub>2</sub> transistor reported by Sharma et al. [26] where the mobility was reported as  $\mu \sim 15.3$  cm<sup>2</sup>/Vs. The reduction in mobility is due to the defects that exist in the thin film which acts as scattering centers which resist the charge conduction. The reason for the low-mobility was further supported with Raman spectra analysis which is shown in Figure 6. The Raman spectra show two active modes at 381 cm<sup>-1</sup> and 406 cm<sup>-1</sup> which represent the E<sub>12g</sub> and A<sub>1g</sub> vibration modes, respectively. Out of these two vibration modes, A<sub>1g</sub> corresponds with the thickness of the layer and A<sub>1g</sub> mode at 406 cm<sup>-1</sup> reveals that the thin film may consist of several MoS<sub>2</sub> sheets interlinked each other. As per the previous reports, the spin-coated thin films consist of several layers of MoS<sub>2</sub> and its bulk counterpart [27, 28].

In general, the surface defects and structural disorders form traps in the form of wrinkles or folds on the surface, creating a small bulk counterpart in MoS<sub>2</sub> thin film [29]. These traps are answerable for the observation of lower mobility in TFT devices. Breakage of S-Mo-S bonds during the synthesis process may lead to these kinds of traps/vacancy defects.

From the obtained results, we noticed that some sophisticated sample preparation techniques such as atomic layer deposition and chemical vapour deposition could be utilized to develop the high purity thin film for ultrafast response electronics devices.

## 4. Conclusion

The electrical transport characteristics of nanoform MoS<sub>2</sub> thin film transistor device were investigated. MoS<sub>2</sub> nanoparticles were prepared using the hydrothermal method. The as-prepared MoS<sub>2</sub> samples were characterized with UV-vis, FT-IR, and X-ray diffraction techniques. Back-gated MoS<sub>2</sub> transistor device was made with silver electrodes as a source and drain. The current-voltage characteristics show a non-linear behaviour. But the observation of symmetry in the I-V curves confirms the nonexistence of the Schottky contact between the thin film and contacts. Transistor characteristic studies further reveal that the TFT device is n-doped while registering the charge neutrality point at the negative bias region. The relationship between gate current and gate voltage with zero gate current shows the good solidarity of transfer characteristic results. The device mobility is calculated as  $\sim 10.2$  cm<sup>2</sup>/Vs, which has a well agreement with the data reported for the MoS<sub>2</sub> transistor. The observation of lower mobility in our MoS<sub>2</sub> TFT device is further plausibly explained with Raman spectra analysis.

## Data Availability

The complete data required for the representations are fully included in the research paper.

## Conflicts of Interest

The authors declare that they have no conflicts of interest.

## References

- [1] S. Kim, J. Nah, I. Jo et al., "Realization of a high mobility dual-gated graphene field-effect transistor with  $\text{Al}_2\text{O}_3$  dielectric," *Applied Physics Letters*, vol. 94, no. 6, article 62107, 2009.
- [2] K. S. Novoselov, D. Jiang, F. Schedin et al., "Two dimensional atomic crystals," *Proceedings of the National Academy of Sciences*, vol. 102, no. 30, p. 10451, 2005.
- [3] M. Chen, Y. Dai, J. Wang et al., "Smart combination of three-dimensional flower-like  $\text{MoS}_2$  nanospheres/interconnected carbon nanotubes for application in supercapacitor with enhanced electrochemical performance," *Journal of Alloys and Compounds*, vol. 696, pp. 900–906, 2017.
- [4] G. Ye, Y. Gong, J. Lin et al., "Defects engineered monolayer  $\text{MoS}_2$  for improved hydrogen evolution reaction," *Nano Letters*, vol. 16, no. 2, pp. 1097–1103, 2016.
- [5] S. V. Prabhakar Vattikuti and J. Shim, "Synthesis, characterization and photocatalytic performance of chemically exfoliated  $\text{MoS}_2$ ," *IOP Conference Series: Materials Science and Engineering*, vol. 317, no. 1, p. 12025, 2018.
- [6] M. Acerce, D. Voiry, and M. Chhowalla, "Metallic 1T phase  $\text{MoS}_2$  nanosheets as supercapacitor electrode materials," *Nature Nanotechnology*, vol. 10, no. 4, pp. 313–318, 2015.
- [7] Y. Liang, R. Feng, S. Yang, H. Ma, J. Liang, and J. Chen, "Rechargeable Mg batteries with graphene-like  $\text{MoS}_2$  cathode and ultra-small Mg nanoparticle anode," *Advanced Materials*, vol. 23, no. 5, pp. 640–643, 2011.
- [8] J. Chen, K. Nobuhiro, Y. Huatang, H. T. Takeshita, and T. Sakai, "Electrochemical hydrogen storage in  $\text{MoS}_2$  nanotubes," *Journal of the American Chemical Society*, vol. 123, no. 47, pp. 11813–11814, 2001.
- [9] A. D. Yoffe, "Electronic properties of some chain and layer compounds," *Chemical Society Reviews*, vol. 5, p. 51, 1976.
- [10] R. Suzuki, M. Sakano, Y. J. Zhang et al., "Valley-dependent spin polarization in bulk  $\text{MoS}_2$  with broken inversion symmetry," *Nature Nanotechnology*, vol. 10, no. 9, pp. 611–617, 2014.
- [11] B. Radisavljevic, A. Radenovic, J. Brivio, V. Giacometti, and A. Kis, "Single-layer  $\text{MoS}_2$  transistors," *Nature Nanotechnology*, vol. 6, no. 3, pp. 147–150, 2011.
- [12] F. Xiong, Z. Cai, L. Qu, P. Zhang, Z. Yuan, and O. K. Asare, "Three-dimensional crumpled reduced graphene oxide/ $\text{MoS}_2$  nanoflowers: a stable anode for lithium-ion batteries," *ACS Applied Materials & Interfaces*, vol. 7, no. 23, pp. 12625–12630, 2015.
- [13] J. Yuan and J. Lou, "Memristor goes two-dimensional," *Nature Nanotechnology*, vol. 10, no. 5, pp. 389–390, 2015.
- [14] P. Qin, G. Fang, W. Ke et al., "In situ growth of double-layer  $\text{MoO}_3/\text{MoS}_2$  film from  $\text{MoS}_2$  for hole-transport layers in organic solar cell," *Journal of Materials Chemistry A*, vol. 2, no. 8, pp. 2742–2756, 2014.
- [15] H. Zhu, Y. Wang, J. Xiao et al., "Observation of piezoelectricity in free-standing monolayer  $\text{MoS}_2$ ," *Nature Nanotechnology*, vol. 10, no. 2, pp. 151–155, 2015.
- [16] O. Lopez-Sanchez, D. Lembke, M. Kayci, A. Radenovic, and A. Kis, "Ultrasensitive photodetectors based on monolayer  $\text{MoS}_2$ ," *Nature Nanotechnology*, vol. 8, no. 7, pp. 497–501, 2013.
- [17] L. Ma, D. N. Nath, E. W. Lee II et al., "Epitaxial growth of large area single-crystalline few-layer  $\text{MoS}_2$  with high space charge mobility of  $192\text{ cm}^2\text{ V}^{-1}\text{ s}^{-1}$ ," *Applied Physics Letters*, vol. 105, no. 7, article 72105, 2014.
- [18] N. Chaudhary, M. Khanuja, and S. S. I. Abid, "Hydrothermal synthesis of  $\text{MoS}_2$  nanosheets for multiple wavelength optical sensing applications," *Sensors and Actuators A: Physical*, vol. 277, pp. 190–198, 2018.
- [19] L. Luo, M. Shi, S. Zhao et al., "Hydrothermal synthesis of  $\text{MoS}_2$  with controllable morphologies and its adsorption properties for bisphenol A," *Journal of Saudi Chemical Society*, vol. 23, no. 6, pp. 762–773, 2019.
- [20] S. Kim, A. Konar, and W. S. Hwang, "High-mobility and low-power thin-film transistors based on multilayer  $\text{MoS}_2$  crystals," *Nature Communications*, vol. 3, p. 1011, 2012.
- [21] J. Pu, Y. Yomogida, K. Liu, L.-J. Li, Y. Iwasa, and T. Takenobu, "Highly flexible  $\text{MoS}_2$  thin-film transistors with ion gel dielectrics," *Nano Letters*, vol. 12, no. 8, pp. 4013–4017, 2012.
- [22] L. Luo, J. Li, J. Dai et al., "Bisphenol A removal on  $\text{TiO}_2$ - $\text{MoS}_2$ -reduced graphene oxide composite by adsorption and photocatalysis," *Process Safety and Environmental Protection*, vol. 112, pp. 274–279, 2017.
- [23] V. Chikan and D. Kelley, "Size-dependent spectroscopy of  $\text{MoS}_2$  nanoclusters," *Journal of Physical Chemistry B*, vol. 106, no. 15, pp. 3794–3804, 2002.
- [24] D. Gao, M. Si, J. Li et al., "Ferromagnetism in freestanding  $\text{MoS}_2$  nanosheets," *Nanoscale Research Letters*, vol. 8, p. 129, 2013.
- [25] K. Chan and W. Chen, "In situ synthesis of  $\text{MoS}_2$ /graphene nanosheet composites with extraordinarily high electrochemical performance for lithium ion batteries," *Chemical Communications*, vol. 47, pp. 4252–4254, 2011.
- [26] D. Sharma, A. Motayed, P. B. Shah et al., "Transfer characteristics and low-frequency noise in single- and multi-layer  $\text{MoS}_2$  field-effect transistors," *Applied Physics Letters*, vol. 107, p. 162102, 2015.
- [27] C. Lee, H. Yan, L. E. Brus, T. F. Heinz, J. Hone, and S. Ryu, "Anomalous lattice vibrations of single- and few-layer  $\text{MoS}_2$ ," *ACS Nano*, vol. 4, no. 5, pp. 2695–2700, 2010.
- [28] S. Baidyaroy and P. Mark, "Analytical and experimental investigation of the effects of oxygen chemisorption on the electrical conductivity of  $\text{CdS}$ ," *Surface Science*, vol. 30, no. 1, pp. 53–68, 1972.
- [29] H. C. Schniepp, J. L. Li, M. J. McAllister et al., "Functionalized single graphene sheets derived from splitting graphite oxide," *Journal of Physical Chemistry B*, vol. 110, no. 17, pp. 8535–8539, 2006.